LUND UNIVERSITY | LTH FACULTY OF ENGINEERING

A journey of growth: β-Ga_2O_3 on GaN and sapphire via Pulsed Laser Deposition

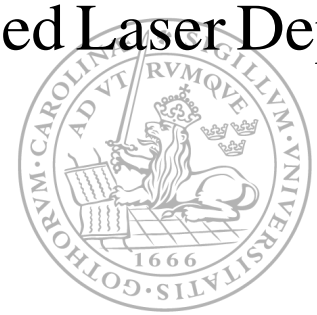

LUNDS UNIVERSITET

Laura de la Fuente Esteban

Thesis for the degree of
Master of Science in Nanoscience

Supervisor: Vanya Darakchieva
Co-supervisor: Andri Dhora

Lund, June 25, 2026

Division of Solid State Physics
Department of Physics
Faculty of Engineering, LTH
Box 118, 221 00 Lund, Sweden

Abstract

The exceptional breakdown field and ultra-wide bandgap of beta-gallium oxide (β-Ga_2O_3) position it as a promising material for next-generation high-power electronics. This thesis systematically investigates the growth behaviour, structural quality, and surface morphology of β-Ga_2O_3 thin films deposited via Pulsed Laser Deposition (PLD) on both c-plane sapphire (Al_2O_3) and MOCVD-grown GaN-on-sapphire templates under identical conditions. Deposition parameters were mapped across a broad experimental matrix, varying substrate temperatures from 500°C to 800°C and oxygen background pressures from 10^{-6} mbar (vacuum) to 10^{-1} mbar. Characterization was performed using spectroscopic ellipsometry, X-ray diffraction (XRD), atomic force microscopy (AFM), and scanning electron microscopy (SEM). Three main parameters were used to assess the overall quality of the films: growth rate, crystal quality, and surface roughness. First, the growth rate evolution is evaluated for all grown layers to delineate the material tendencies with respect to the growth conditions. Next, a comparative structural analysis of the $(\bar{2}01)$ crystal orientation is presented for both substrates to isolate how growth parameters influence overall crystalline quality. To overcome severe interfacial degradation caused by premature GaN substrate oxidation under oxygen-rich environments, a two-step deposition process utilizing an inert Argon (Ar) sacrificial buffer layer is introduced. Finally, the surface topography is analyzed to establish a correlation between substrate temperature and surface roughness (RMS). Together, these structured analyses provide a comprehensive framework for understanding β-Ga_2O_3 thin films deposited via PLD.

Popular Summary

It is a freezing winter day in Lund. The snow is slowly falling, and as it touches the ground, you notice a snowflake form. It is symmetric and beautifully ordered: it crystallized. This is a rare sight in a city where *slask* (slush) reigns. You snap a picture to send to your mum and quickly check the weather app: -5°C. The next day you wake up, and it's even colder, darker, a bit more humid even. Charming Lund. On your way to university, you spot it again: a snowflake. This time, though, something is different. Its shape and symmetry have completely changed. You snap a new picture and, comparing both, you notice that while both are flawlessly ordered, their shape, size, and structural perfection are entirely different. That must be it! The atmospheric conditions must have changed it all.

In physics, any solid material whose atoms are arranged in a highly ordered, three-dimensional pattern is called a crystal. You interact with them every day: your diamond engagement ring, cooking salt, or the tip of your pencil (though some of them are more expensive than others).

This thesis explores the formation of a very specific crystal: β-Ga_2O_3 (beta-gallium oxide). While it might not be as beautiful as snowflakes at plain sight, this material possesses great technological powers. It is capable of controlling electricity under extreme conditions. The ultimate advantage of β-Ga_2O_3 lies in its ability to sustain very high voltage while reducing energy losses when an electronic device is running.

Just like snowflakes, the formation of this crystal is highly sensitive to its environment. Therefore, to achieve its full potential, specific techniques are needed to fine-tune and customize its growth conditions. To grow these gallium oxide crystals, a simple but effective method is used: Pulsed Laser Deposition (PLD). To picture how it works, let's step back out into the *slaskigt* streets of Lund. Think about stomping through heavy *slask*. With every step you take, the energy from your foot sends the *slask* flying through the air, unfortunately landing on the bottom of your pants, leaving a distinct wet stain. In the lab, this process is recreated on an atomic scale:

- The foot: a high-power pulsing laser.
- The *slask*: a block of (not crystalline) gallium oxide material.
- The pants: a specialized base material called a substrate.

When the laser strikes the target material, it acts just like your foot hitting the *slask*, blasting a cloud of atoms into the air. These flying particles travel across an enclosed chamber and land on the substrate. By carefully tuning the temperature and pressure of this environment, it is possible to form highly ordered and crystalline β-Ga_2O_3.

Hence, this work aims to pave the way for next-generation electronics by identifying the optimal atomic "weather conditions" for high-quality beta-gallium oxide growth.

Resumen Popular

Es un día frío en Lund. La nieve está cayendo y, al tocar el suelo, te percatas de que un copo de nieve se ha formado. Es simétrico y bien estructurado: ha cristalizado. Un suceso cuanto menos extraño, en esta ciudad en la que el aguanieve reina. Le haces una foto para enseñársela a tu madre y rápidamente miras la aplicación del tiempo: -5°C. Al día siguiente, te despiertas y hace aún más frío, está aún más oscuro e incluso, el ambiente se siente más húmedo. Lund es encantadora. En tu camino a la universidad, lo vuelves a ver: un copo de nieve. Sin embargo, esta vez, algo ha cambiado. Su forma y simetría son diferentes. Haces otra foto y, al comparar ambos copos, notas que aunque los dos son perfectos, su forma, tamaño y estructura son completamente diferentes. ¡Eso es! Las condiciones atmosféricas han debido de cambiarlo todo.

En física, cualquier material sólido cuyos átomos están dispuestos en un patrón tridimensional altamente ordenado se denomina cristal. Tú interactúas con ellos constantemente: tu anillo de pedida de diamantes, la sal de cocinar o la punta del lápiz (aunque algunos son más caros que otros).

Esta tesis explora la creación de un cristal sumamente específico: β-Ga_2O_3 (óxido de galio beta). Si bien puede que no sea tan bonito como los copos de nieve a simple vista, este material tiene unas propiedades tecnológicas envidiables. Es capaz de controlar la electricidad en condiciones extremas. Su mayor ventaja es su capacidad para soportar altos voltajes, reduciendo al mismo tiempo las pérdidas energéticas cuando un aparato eléctrico está encendido.

De la misma manera en la que sucede con los copos de nieve, la formación de este cristal es realmente sensible a su entorno. Por lo tanto, se necesitan técnicas específicas para calibrar y optimizar las condiciones de crecimiento del cristal y así alcanzar su máximo potencial. Para hacer crecer estos cristales de óxido de galio, se ha utilizado un método simple pero efectivo: deposición por láser pulsado (PLD). Para entender cómo funciona, volvamos a las calles de Lund, llenas de aguanieve. Piensa en pisotear el aguanieve. A cada paso que das, la energía de tu pisada manda el aguanieve despedido por el aire y desafortunadamente te acaba manchando el bajo del pantalón. En el laboratorio, este proceso se recrea a escala atómica:

- El pie: un láser de gran potencia.
- El aguanieve: un bloque de óxido de galio (no cristalino).
- Los pantalones: un material base llamado sustrato.

Cuando el láser golpea el bloque de material, funciona simplemente como tu pie pisoteando el aguanieve, impulsando una nube de átomos por el aire. Estas partículas voladoras viajan por una cámara cerrada y se depositan en el sustrato. Ajustando la temperatura y la presión del entorno es posible formar β-Ga_2O_3 cristalino.

Por lo tanto, este trabajo pretende allanar el camino para la electrónica de próxima generación mediante la búsqueda de las “condiciones meteorológicas” atómicas óptimas para el crecimiento de óxido de galio beta de alta calidad.

Acknowledgements

First of all, I want to thank **Andri** for his profound support, knowledge, and care. Your time and effort have been immensely valuable to me and I will always carry the good lessons, the advice -*the good and the bad*- and the wisdom you decided to share with me.

This work would not have been possible without **Vanya Darakchieva**, who embraced the young scientist in me and provided me with numerous opportunities to learn. I appreciate the openness and charisma you radiate. It has been great to have such an admirable role model in this field.

To my friends, **Anna, Rafaela and Sophie**, thanks for the support and for being the listeners of my misfortunes. I feel incredibly lucky to have found you in my way. Sharing this life chapter with you has made every day funnier, more bearable and human. It is truly moving to have you next to me.

Noah, you have been a great office companion and I will miss our closed-door conversations. I admire your directness, boundaries and humour. May we meet again.

A special mention to **the people at FTF** and **Dan**, for making my stay in the division more enjoyable and welcoming me with open arms. Thanks for the coffee, the fika and the laughs.

To my **family**, especially my mum and my grandma, for allowing me to disappear for days and call back. I am sorry my phone is always on silent. You are the pillars of any work I will ever do. **Pipo**, you raised me and I miss you. Anything I'll write will always be dedicated to you.

A mi familia, especialmente a mi madre y a mi abuela, por permitirme desaparecer durante días y devolver las llamadas perdidas. Perdón por tener el móvil en silencio. Sois los pilares de cualquier proyecto que haga. Pipo, tú me has criado y te echo de menos. Todo lo que escriba estará dedicado a ti.

Finally, thank you, **Sara**, for being such a compassionate and supportive partner. These two years' successes and failures have been better just because you were next to me. Your patience, love and care have carried me along the way.

You will never know where the rock bottom really sits.

Contents

1 | Introduction

Materials limit and expand the possibilities of technology. The discovery and understanding of semiconductor materials marked the revolution of electronics, which unlocked key capabilities such as precise switching and amplification of signals and light conversion. Since the invention of the first ever transistor in 1947, the industry has evolved at an extremely fast pace. Nowadays, in the era of transport electrification, quantum computing, and energy efficiency, novel and innovative solutions are more necessary than ever.

For a long time, silicon (Si) has reigned as the most reliable, available, and cheap semiconductor for photovoltaics, power, and optoelectronics; partly due to its exceptional properties, partly due to its extensive research and development. This is particularly true for transistors and regular electronics. However, in the field of power electronics, new challenges have emerged in recent years. As technology evolves and industry paces up, new semiconductors are required to support higher voltages and greater energy efficiency. New engineering solutions are necessary to minimize energy losses across every stage of the electrical supply chain. This is particularly true for devices such as Schottky barrier diodes, field-effect transistors, and other devices such as photodetectors. Therefore, the investigation of new materials capable of operating beyond the theoretical limits of Si is essential for enabling the next generation of high-power electronics.

In this work, the growth of β-Ga_2O_3 is investigated. This crystalline semiconductor has been known for a while due to its ultra-wide bandgap and exceptional electrical properties, making it a promising candidate for high-power electronics. In theory, thanks to its ultra-wide bandgap, β-Ga_2O_3 foreshadows reduced device sizes, faster switching, and superior energy efficiency compared to Si-based devices. While other ultra-wide bandgap semiconductors (UWBG), such as Aluminium Nitride (AlN), and established wide bandgap semiconductors (WBG), such as Gallium Nitride (GaN) and Silicon Carbide (SiC), are being explored for next-generation power electronics, β-Ga_2O_3 occupies a unique position. In contrast to its counterparts, β-Ga_2O_3 is the only UWBG material that can be synthesized from the melt for high-quality, large area native substrates. This semiconductor presents, as well, a wide range of controllable n-type doping (10^{15}-10^{20} cm^{-3}), not attainable in other WBG and UWBG [60]. Furthermore, metal oxides, in general, provide superior stability under harsh environmental conditions [11]. Consequently, research into β-Ga_2O_3 is of significant interest due to its potential to transform power electronics. Nevertheless, as an emerging material, it also presents difficulties. Two primary challenges stand out: a notoriously poor thermal conductivity and the inherent difficulty of growing thick, high-quality layers at high growth rates.

The potential of β-Ga_2O_3 lies in its application for vertical power devices, characterized by a vertical, through-bulk current flow. Exploiting the high theoretical breakdown field of β-Ga_2O_3 allows high voltages to be sustained across the device's drift layer. Furthermore, due to this exceptional material property, chip size reduction is possible, particularly for the drift layer [11]. This directly translates into low on-state Ohmic losses, thereby maximizing overall device efficiency. All in all, β-Ga_2O_3 vertical devices open the possibility for more energy- and cost-efficient power electronics applications.

Other epitaxial techniques have demonstrated successful growth of good crystal quality β-Ga_2O_3, including MOCVD [53] and MBE [60]. Pulsed Laser Deposition (PLD) is used in this work

as a benchmark tool for foundational β-Ga_2O_3 growth research. This technique is known for facilitating high-quality epitaxial growth while ensuring the stoichiometric transfer of material from target to substrate. Furthermore, it offers high tunability and control over growth parameters, thereby facilitating precise optimization. Overall, PLD represents an excellent method for experimentation, prototyping and understanding of complex materials.

Despite the inherent benefits of homoepitaxial growth, bulk substrate costs are prohibitively high. In order to bypass this bottleneck, heteroepitaxy on foreign substrates has become a valuable, scalable and cost-effective alternative for initial research development. Throughout this thesis, sapphire (Al_2O_3) and GaN serve as templates for β-Ga_2O_3 growth. On the one hand, sapphire is a mature, low-cost substrate. On the other hand, GaN-on-sapphire combines the low cost and scalability of sapphire with the mature electronic functionality and high carrier mobility of GaN, providing a versatile platform for advanced electronic and photonic devices. However, this approach introduces other scientific challenges: the structural integration of β-Ga_2O_3 onto different crystal geometries induces lattice mismatch and defects. Therefore, it is key to understand the optimal growth conditions required to obtain high-quality crystals at a high growth rate.

In this work, growth of β-Ga_2O_3 on sapphire and GaN-on-sapphire templates under identical conditions is investigated. This approach aims to provide a clearer understanding of the material's growth behaviour on GaN, as well as to determine the key differences between the growth on both substrates. Furthermore, by exploring the introduction of buffer layers, improved crystallinity on GaN is demonstrated. Finally, the relationship between surface roughness and substrate temperature on GaN was investigated. As a result of this exploratory work, other key characteristics and findings unique to β-Ga_2O_3 are presented.

2 | Theoretical Framework

2.1 | Semiconductor Physics of Ga_2O_3

2.1.1 | Crystal Structure

To describe a crystal structure, one must look at the smallest repeating unit of the material: the unit cell. This unit cell is defined by three lattice vectors ($\vec{a}$, $\vec{b}$, and $\vec{c}$) and their respective angles (α, β, and γ). Crystal structures are classified into 7 different crystal systems according to its unit cell geometry: cubic, tetragonal, rhombohedral, hexagonal, orthorhombic, monoclinic and triclinic.

Ga_2O_3 exists in five different polymorphs: α, β, γ, δ, and ϵ [11, 18]. Each phase is defined by its specific unit cell structure and electronic band alignment. Owing to its thermodynamic stability, the β polymorph is the most extensively researched. Specifically, β-Ga_2O_3 presents a base-centered monoclinic crystal structure (Figure 2.1). In this arrangement, the defining vectors of the unit cell, $\vec{a}$, $\vec{b}$, and $\vec{c}$, possess different lengths, and the monoclinic angle β differs from the orthogonal α and γ angles (see Table 2.1).

Table 2.1: Unit cell parameters of β-Ga_2O_3 [18, 62].

$\vec{a}$ (Å)	$\vec{b}$ (Å)	$\vec{c}$ (Å)	β	$\alpha = \gamma$
12.214	3.0371	5.7981	103.83°	90°

Inside of the cell, 20 atoms are found [11, 50]. As illustrated in Figure 2.1, β-Ga_2O_3 consists of two distinct Ga sites (Ga_I, Ga_{II}) and three O sites (O_I, O_{II}, O_{III}). The Ga_I atoms bond tetrahedrally with four oxygen ions (1 O_I, 1 O_{II}, and 2 O_{III}), while Ga_{II} atoms coordinate octahedrally with six oxygen ions (2 O_I, 3 O_{II}, and 1 O_{III}).

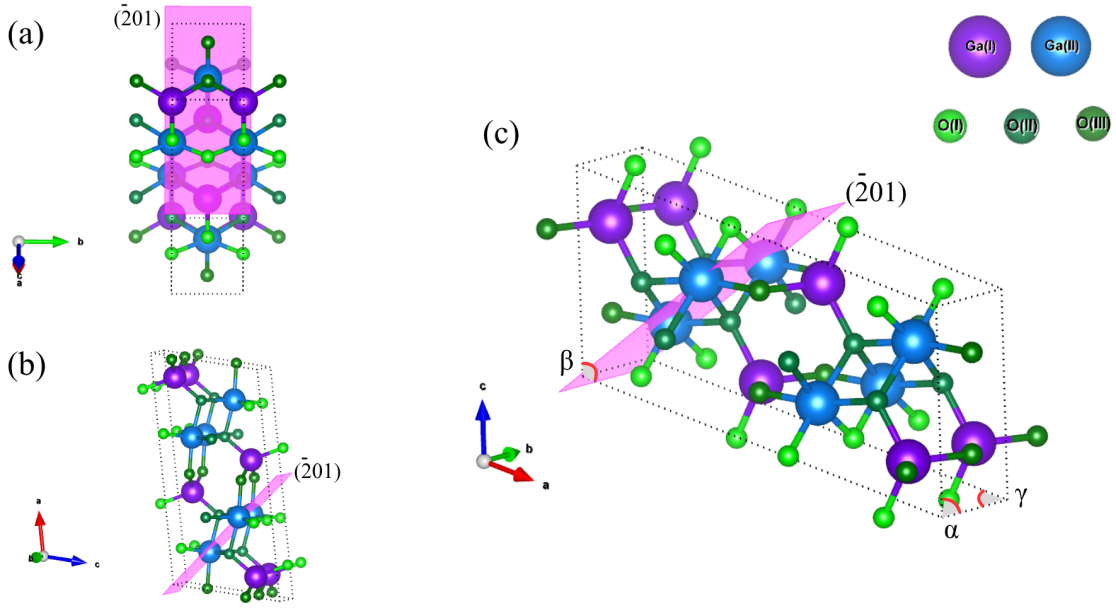

Figure 2.1: Schematic illustration of β-Ga_2O_3 unit cell.

2.1.2 | Material Properties

The band structure of β-Ga_2O_3 has been previously characterized using various methods [11]. Although generally classified as an indirect semiconductor, the minor energy difference between reported direct and indirect bandgaps (at Γ) has led researchers to describe the material as a *pseudo-indirect* [31]. With a bandgap energy of 4.5-4.9 eV [11, 23], β-Ga_2O_3 is settled as an ultra-wide bandgap semiconductor, exceeding bandgap values of the more established WBG such as SiC and GaN [23].

The electronic band structure of β-Ga_2O_3 stands out due to a virtually flat dispersion energy at the valence band (VB) maximum, leading to a very high hole effective mass. Conversely, a strong dispersion at the conduction band (CB) minimum leads to the opposite effect: low electron effective mass [50, 11, 60].

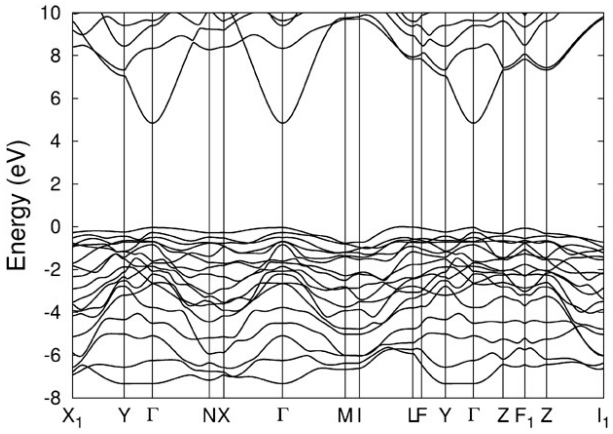

Figure 2.2: Electronic band structure of Ga_2O_3 [30].

The effective mass (m^*) is an intrinsic property of materials that governs the mobility of carriers (μ). Mathematically, $\mu = e\tau/m^*$, where τ is the mean time between collisions. Therefore, it can be observed that the inverse relationship between μ and m^* constrains the mobility of carriers. Besides, the conductivity of the material is directly proportional to this mobility. Namely,

$$\sigma = e(n\mu_n + p\mu_p)$$

In practice, undoped β-Ga_2O_3 usually presents n-type conductivity, due to unintentional n-type doping and defects [11, 60]. This behaviour has also been observed in other wide bandgap oxides such as SnO_2 or ZnO [42, 21]. At the same time, p-type conductivity remains a significant challenge. Similar to other metal oxides [11], the difficulty stems from the electronic structure of the valence band and native donor defects [40]. Specifically for β-Ga_2O_3, the high hole effective mass and the self-trapping of holes in the bulk hinder efficient p-type conductivity, making it impractical to realize [60].

Compared to the established WGB, β-Ga_2O_3 has a significantly theoretical higher breakdown field (8 MV/cm) [23, 18]. This advantage allows for a higher tolerance to high electric fields, and, consequently, for the possibility of smaller devices, specifically the drift region thickness [57]. The breakdown field is fundamentally linked to the material's bandgap and follows a simple power-law: $\epsilon_{crit} \propto E_g^{\gamma}$, where the exponent typically ranges values between 2 and 2.5 [60, 43].

To quantify the suitability of these materials for power electronics, semiconductor performance is usually evaluated using Baliga's Figure of Merit (BFOM) [17]. Here, unipolar transistor's performance is theorized based on the on-state resistance and the breakdown voltage at low frequencies [1, 17], following

$$BFOM = \epsilon \mu E_g^3$$

where ϵ is the dielectric constant, μ is the mobility and E_g is the material's bandgap. Because the figure of merit scales with the third power of the bandgap, β-Ga_2O_3 offers a massive theoretical advantage over its predecessors. By improving the strict trade-off between breakdown voltage and conduction loss, β-Ga_2O_3 can sustain significantly higher blocking thresholds while simultaneously minimising specific on-resistance compared to narrower-bandgap semiconductors. A clear comparison of the most-researched UWBG materials can be observed in Figure 2.3.

The ultra-wide bandgap of β-Ga_2O_3 not only allows for great electronic advantages but also optical. This material presents optical transparency across the visible and into the UV spectrum [11, 31]. This property, combined with its high n-conductivity, poses β-Ga_2O_3 as a good candidate for various optoelectronic applications, including photodetectors or transparent conductive oxide electrodes, among others [11].

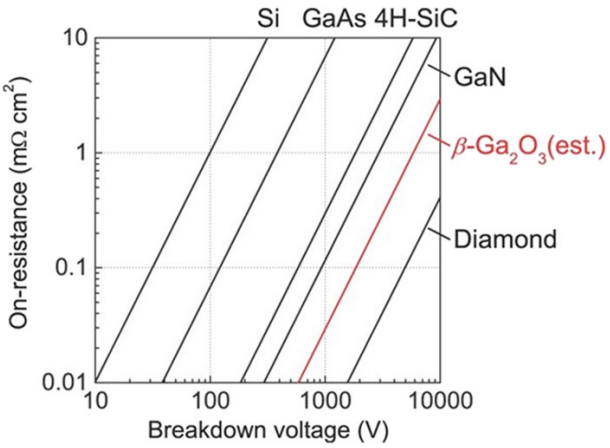

Figure 2.3: BFOM for well-researched WBG and UWBG semiconductors [60].

Despite its advantages, a noteworthy challenge for β-Ga_2O_3 is its low thermal conductivity. This intrinsic property describes the capacity of a material to conduct heat across a temperature gradient [11]. Fundamentally, this characteristic imposes the power operation limit for any device. As a candidate for the next generation of power electronics, β-Ga_2O_3 is subjected to high currents and voltages, leading to substantial resistive heating. Without efficient energy dissipation, thermal degradation accelerates, and the devices' performance hinders as electron mobility and electron saturation velocity are reduced [50]. Multiple studies have reported Ga_2O_3 poor thermal conductivity, pointing at the large and complex phonon scattering phase space (i.e. set of combinations of phonon-phonon interactions that obey the energy and momentum conservation rules) [50, 11, 44].

2.2 | Epitaxy Fundamentals

Like many terms in modern science, *epitaxy* comes from the Greek $\epsilon\pi\iota$ (*epi-*, upon, on) and $\tau\alpha\xi\iota\sigma$ (*-taxis*, arrange, order) [27, 33]. This translates to the ordered and oriented growth of a crystal material on a single-crystalline substrate. Epitaxy is broadly categorized into two types, depending on the relationship between the substrate and the grown material. If both materials are the same, the process is referred to as *homoepitaxy*. On the contrary, if substrate and layer differ, it is known as *heteroepitaxy*. In any of these cases, the process entails the mimicking of the substrate's orientation in the grown layer, also referred to as epitaxial orientation. Two lattice planes grow parallel to each other, arranging their atomic structures at the junction to match. Regardless, in heteroepitaxy, the matching of both elements is not perfect. A lattice misfit (f) exists. Hence, the relative difference between the lattice constants can be defined as

$$f = \frac{a_S - a_L}{a_L} \tag{2.1}$$

where a_S and a_L are the lattice constants of the substrate and epitaxial layer, respectively.
The relevance of this parameter was first reported by Louis Royer in 1928 [27]. Based on experimental observations, he reported that the crystal planes of substrate and layer must not have a lattice misfit greater than 15% to achieve epitaxial growth [33]. This and other Royer rules are still relevant to this day, although further research has expanded the limits for achievable misfits between materials.

2.2.1 | Reaction thermodynamics

Thermodynamics in epitaxy is used as a tool to determine the stability and composition of different phases in the equilibrium state. At constant temperature and pressure, equilibrium is defined as the state in which the Gibbs free energy, G, is minimal. This parameter is defined as

$$G = U + PV - TS$$

where U is the internal energy, P is the pressure, T is the temperature and S is the entropy.

The changes of energy in a system caused by the addition or removal of a particle can be described by the so-called chemical potential. Mathematically, this parameter is defined as the partial derivative of the Gibbs free energy with respect to the number of particles of species n_i at fixed temperature and pressure:

$$\mu_i = \left(\frac{\partial G}{\partial n_i}\right)_{T,P,n_i}$$

Epitaxy is fundamentally a controlled phase transition from an initial (gas or liquid) phase to a crystalline solid phase. In this context, the differences between the chemical potentials of each phase are the primary thermodynamic driving force for growth [46]. Under thermodynamic equilibrium conditions, these two co-existing chemical potentials, μ_α and μ_β, are equal. However, in order to induce crystallization, the system must move away from equilibrium such that the chemical potential in the target phase (β) is smaller than that in the initial phase (α) [33].

$$\mu_\beta(P) < \mu_\alpha(P)$$

The resulting difference, $\Delta\mu = \mu_\beta - \mu_\alpha$, represents the driving force for crystallization [33]. While this driving force can be induced by supercooling (ΔT), in this context of vapour-phase

epitaxy, it is induced by supersaturation ($\Delta P = P - P_e$) at a constant temperature. Here, P is the actual pressure and P_e is the equilibrium vapour pressure. The chemical potential difference can be expressed mathematically by integrating $\Delta\mu$ over pressure. By treating the vapour as an ideal gas, the relationship follows

$$\Delta\mu(\Delta P) = -RT \ln\left(\frac{P}{P_e}\right) \tag{2.2}$$

Hence, the chemical potential is approximately proportional to the natural logarithm of the supersaturation ratio P/P_e of the initial gas phase α.

The surface energy is also an important concept for understanding the initial growth morphology. For 3D growth, spherical nuclei may develop on top of the substrate. In this scenario, three actors come into play: the surface energy of the interface nucleus-ambience (γ_{an}), the interface substrate-ambience (γ_{as}), and that between nucleus and substrate (γ_{ns}). The surface energies represent the energies required to create a new unit area at the interface between each two phases. Young's relation describes the interplay between the three surface energies:

$$\cos\theta = \frac{\gamma_{as} - \gamma_{ns}}{\gamma_{an}} \tag{2.3}$$

where θ is the wetting angle between the solid substrate and the interface of the nucleus (Figure 2.4). This angle determines the shape of the cap and may vary between 0 and 180° [33]. Furthermore, the energy barrier to nucleation is dependent on the wetting angle, with smaller values facilitating the process.

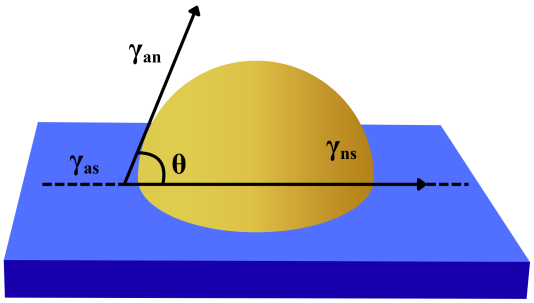

Figure 2.4: Nucleus created on a substrate and respective surface energies.

Specifically for this work, the simplest case of GaO synthesis from a vapour phase can be described as:

$$\begin{aligned} 2\,\mathrm{Ga(a)} + \mathrm{O(a)} &\longrightarrow \mathrm{Ga_2O(a)} \\ \mathrm{Ga_2O(a)} + 2\,\mathrm{O(a)} &\longrightarrow \mathrm{Ga_2O_3(s)} \end{aligned} \tag{2.4}$$

The growth of Ga_2O_3 is primarily driven by the balance between the incorporation of adatoms and the desorption of volatile species, specifically Ga_2O. Therefore, to favour crystal growth and overall growth rate, it is required to use high precursor fluxes of $Ga_{(g)}$ and $O_{2(g)}$ while maintaining relatively low temperatures [54].

In thermodynamic terms, supplying precursors at pressures well above their equilibrium pressures and at low growth temperatures allows for the suppression of Ga_2O_3 decomposition. While these

conditions maximize the incorporation rate, they often come at a cost to the final crystal quality and surface morphology, as lower temperatures can limit the ability of adatoms to reach optimal lattice sites. A more comprehensive, kinetic analysis of these desorption and incorporation regimes will be presented in the following sections.

2.2.2 | Nucleation

Epitaxial growth begins with the formation of small clusters (nuclei) of the new solid [33]. The formation of these nuclei is governed by a change of Gibbs energy (ΔG_N), which is a battle between the contribution of two opposing terms: ΔG_V, which is the energy liberated in proportion to the formation of the nucleus volume, and ΔG_S, which is the energy consumed to create the interface between the nucleus and the metastable surrounding phase.

Because of the energetically unfavourable formation of the interface, the Gibbs energy initially increases until the volume term counterbalances this effect due to fast nucleus growth [33]. Eventually, the system reaches a maximum energy state at a specific nucleus radius known as the critical radius r^*. Under supersaturation conditions, the critical radius is expressed as

$$r^* = \frac{2\gamma\upsilon}{\Delta\upsilon_e \Delta P}$$

where γ is the surface free energy, υ is the molar volume of the new phase, $\Delta\upsilon_e$ is the difference in molar volume between the phases, and ΔP is the supersaturation. For clusters that do not reach this specific radius, instability dominates and they tend to disband [33].

The necessary energy to surpass this critical radius and ensure nuclei stability and consequential growth is referred to as the nucleation energy barrier, ΔG_N^*. This barrier acts as the activation energy required so that the system can initiate the phase transition. Specifically, in heteroepitaxy, the presence of a substrate presents preferential sites to reduce this barrier by a factor f, which depends on the wetting angle θ. This heterogeneous 3D nucleation barrier is defined as:

$$\Delta G^*_{N,hetero} = \frac{16\pi}{3} \frac{\gamma_{an}^3 \upsilon^2}{(\Delta g)^2} f$$

where γ_{an} is the surface energy between the ambient phase and the nucleus, and Δg is the change in molar Gibbs energy.

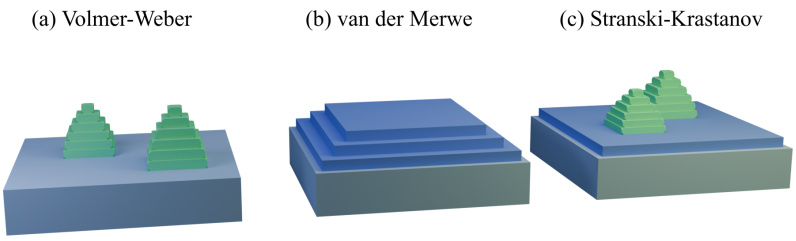

Figure 2.5: Schematic of the three growth modes: (a) Volmer-Weber, (b) van der Merwe, and (c) Stranski-Krastanov.

Following Young's relation 2.3, three different growth modes can happen depending on the interplay between the system's surface energies (see Figure 2.5). Ideally, growth would follow a

layer-by-layer model, where the layer atoms are substantially more attracted to the substrate than to each other [33]. The growth would proceed in an atomically flat 2D manner, with a wetting angle of 0 or if the surface energy of the ambience-substrate interface exceeds the sum of the other two. This mode, referred to as Frank-Van der Merve, follows,

$$\gamma_{as} \geq \gamma_{ns} + \gamma_{an} \tag{2.5}$$

completing the wetting of the layer on the substrate surface. A different mode can occur while complete wetting is achieved if a perceptible misfit between both materials exists [27]. Growth can follow Stranski-Krastanow mode (or layer+island) in which condition 2.5 is met only for the first or few first monolayers. In this case, after exceeding some critical coverage thickness, the formation of 3D islands occurs. This change may be caused by the the gradual accumulation of strain in the grown layer, which relaxes elastically, resulting in the formation of 3D islands [33]. The complete wetting condition falls and

$$\gamma_{ns} \geq \gamma_{as} + \gamma_{an} \tag{2.6}$$

is met. If only condition 2.6 drives growth, then Volmer-Weber growth takes place. In this mode, the layer atoms have a stronger attraction between each other than to the surface of the substrate [33]. The layer does not wet the surface, with the wetting angle being π. The result is solely three-dimensional island growth.

2.2.3 | Kinetics and Surface Processes

Although the three thermodynamically explained growth modes occur in reality, kinetics must also be taken into account when describing growth. On short time scales and far away from macroscopic considerations, epitaxial kinetics usually offer a more appropriate description.

As the input flow of precursors impinges on the substrate, atoms may adsorb on the surface. In this case, they are referred to as *adatoms*, which may undergo surface diffusion depending on the kinetic energy they carry and the presence of defects and energetically favourable sites. Throughout this mechanism, they join other adatoms to nucleate or incorporate into already-formed islands. Depending on the temperature and input precursor flux, atoms can just re-evaporate after a mean residence time. Desorption may also happen if a nucleus can not attain the critical size [33].

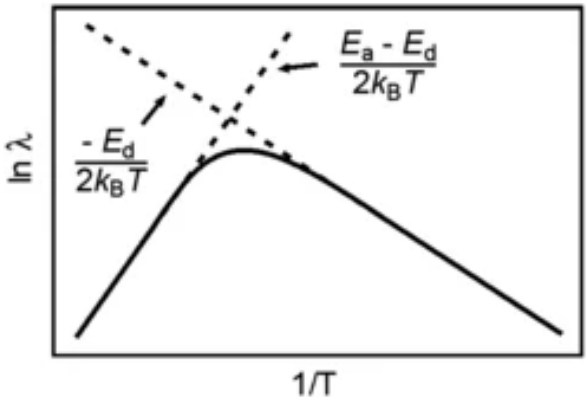

Figure 2.6: Temperature dependence of diffusion length, illustrating the high-temperature desorption regime (left) and the low-temperature incorporation regime (right) [33].

As shown in [33], low growth temperatures suppress adatom desorption in favour of incorporation. Under these conditions, the surface diffusion length λ is limited by the rate of thermally activated hopping frequency υ_d and increases exponentially with temperature according to:

$$\upsilon_d = \upsilon_{d0} \exp\left[(-E_d)/(k_B T)\right] \tag{2.7}$$

where υ_{d0} is the pre-exponential attempt-rate constant and E_d is the diffusion barrier energy. At higher temperatures, desorption dominates, and λ is expected to decrease exponentially according to

$$\lambda = \lambda_0 \exp\left[(E_a - E_d)/(2k_B T)\right] \tag{2.8}$$

where E_a is the adsorption energy. These two temperature regimes are illustrated in Figure 2.6.

Films with the highest crystal quality tend to occur at long diffusion lengths [33]. For adatoms to diffuse along the surface and incorporate at energetically favourable lattice sites, they must surpass the diffusion barrier E_d. This in turn results in smooth surface morphology and high crystal quality, necessary features for optimal electrical material properties [33]. However, this is expected to happen at the expense of the growth rate. To increase the incorporation rate, the precursor flux needs to be elevated, which subsequently increases the density of stable clusters nucleating randomly across the surface. As the density of these clusters rises, the mean time an adatom spends diffusing before being captured (τ) is reduced. Because the surface diffusion length is defined as $\lambda = \sqrt{D\tau}$, where D is the material-dependent diffusivity, this reduction directly shortens λ. Consequently, higher growth rates suppress long-range surface diffusion. Therefore, a trade-off between crystal quality and growth rate exists.

2.2.4 | Defects

From entropic considerations, epitaxy can never lead to perfectly ordered and smooth layers. In reality, several defects develop at greater concentrations in the case of heteroepitaxy. Defects include point defects, such as vacancies, and dislocations, which develop as a result of strain energy build-up and subsequent plastic relaxation [33].

Each material is inherently defined by its lattice vectors and constant. For heteroepitaxial growth, this brings challenges as both substrate and layer, need to accommodate the differences in lattice structure and thermal coefficients. Preferentially, the by-product of this matching between both layers would result in the so-called pseudomorphic growth. Pseudomorphic layers are formed when the resulting strain from the misfit is homogeneous, fitting precisely the atomic template of the substrate. The film has no misfit dislocation, but it accumulates stress [33].

The result of the stress accumulation induces the strain, which acts as the primary source for the appearance of misfit dislocations once the critical thickness is achieved [48]. There exists a trade-off between the suppression of misfit dislocation and the total elastic strain energy accumulated by the system. As the film thickness increases, it reaches a point of no return. Past the critical thickness, strain plastically relaxes, forming structural defects [33]. The heterostructure looks for an energetically favourable state to relieve stress by forming misfit dislocations. Therefore, strategies to extend the characteristic critical thickness of heterostructures are key. Multiple approaches have been explored. In the context of this work, only the introduction of buffer layers is discussed.

The use of buffer layers to reduce the presence of misfit dislocations is a widely applied method [33, 15, 2]. Particularly, such a layer seeks to trap and prevent the propagation of dislocations into the main film, allowing for a layer with a lower misfit density to grow on top [33]. This, in theory, should relieve strain and enhance the nucleation process, enabling a better quality film [2].

Aside from misfit dislocations, other structural defects can be encountered. In this work, neither the density nor the type of defects are studied. Therefore, for the sake of simplicity, only misfit dislocations are considered with regard to the introduction of buffer layers.

2.2.5 | Substrates for Ga_2O_3 heteroepitaxy

In this work, two different substrates have been used: sapphire (Al_2O_3) and gallium nitride on sapphire (GaN/Al_2O_3).

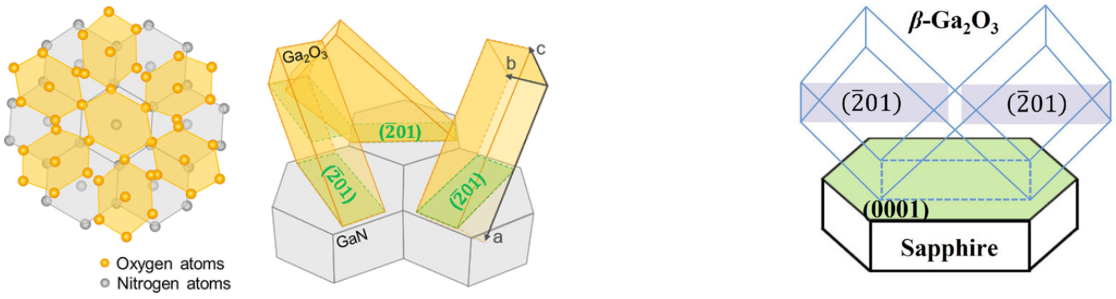

(a) [39] **(b)** [58]

Figure 2.7: Matching of β-Ga_2O_3 unit cell on (a) GaN and (b) sapphire.

Sapphire substrates are widely used for heteroepitaxial growth due to their technological maturity, thermal stability, low cost and wide availability. Moreover, this crystal is compatible with multiple orientations, allowing for the tuning of growth behaviour depending on scientific goals. Here, single-crystalline c-plane sapphire is used. The (0001) plane from the hexagonal lattice (Figure 2.7b) serves as the growth template for β-Ga_2O_3. The growth between both crystals is generally favourable. In particular, the lattice mismatch between them is reported to be around 6.6% [29, 40]. The lattice alignment is also promoted due to similarities in atomic arrangement [25]. β-Ga_2O_3 preferentially orients along the $(\bar{2}01)$ plane with the (0001) plane of the substrate [40]. This orientation allows for a favourable matching of oxygen atoms between both planes and, as growth occurs, gallium can bond to the sapphire oxygen atoms almost without feeling great differences [29, 40]. Hence, minimizing lattice and structural mismatch. Although atomic matching is relatively good, there exists a symmetry mismatch. Single crystalline β-Ga_2O_3 presents a two-fold symmetry structurally, but influenced by the six-fold symmetry of sapphire, it is altered, showcasing six-fold twins [25].

As discussed in other studies [39, 5], the use of GaN in combination with β-Ga_2O_3 is proposed as an escape way to overcome the p-type β-Ga_2O_3 challenge by introducing a p-GaN/n-Ga_2O_3 heterojunction. This heteroepitaxy is of great interest for the development of power electronics and optoelectronic devices because of GaN's outstanding luminescence and conduction properties [15, 4]. Throughout this work, MOCVD-grown GaN-on-sapphire is used. GaN-on-sapphire takes the (001) orientation on c-plane sapphire. In this case, β-Ga_2O_3, just as for sapphire, tends to orient along the $(\bar{2}01)$ plane on top of GaN (Figure 2.7a) [15, 39]. The specific lattice

mismatch for $(\bar{2}01)||(0001)$ β-Ga_2O_3 on GaN is slightly lower than on sapphire, reaching 4.7% [25, 28]. This figure is achieved because in the $(\bar{2}01)$ plane, oxygen atoms pseudo-replicate the hexagonal nature of GaN, adapting to the nitrogen atoms of the substrate [39, 22]. Again, as in sapphire, β-Ga_2O_3 presents a six-fold symmetry on GaN due to the intrinsic sixfold nature of the wurtzite lattice [39].

2.3 | Pulsed Laser Deposition

Pulsed Laser Deposition (PLD) is a physical vapour deposition technique used for thin-film growth [14]. Unlike chemical deposition methods that rely on gaseous or liquid precursors, PLD inherently utilizes sintered solid targets. The mechanics of the PLD deposition are, in theory, quite simple. A laser is pointed at a solid target, which contains the deposition material, and hits its surface in nanosecond pulses, removing material. The removed surface is ejected in the form of a plasma plume, which contains the species (precursors) for growth and expands towards the substrate positioned on top of the target. As these precursors arrive at the surface of the substrate, they adsorb to form a continuous thin film. The growth process can also be complemented with a background passive or reactive gas [56].

This technique provides significant advantages in terms of film purity and stoichiometric control. PLD enables growth of highly-pure thin films across a wide range of pressures: from ultra-high vacuum to mbar readings [41]. Compared to alternative growth methods, PLD allows growing highly complex materials with exceptional stoichiometric precision [41, 14], making it a great technique to experiment with novel materials. In practice, the primary limitation is simply whether the material of choice can be fabricated into a target with high purity and proper density [56]. Due to its large number of controllable parameters, it is fairly easy to optimize growth rates [56, 36]. However, although PLD allows for great tunability (e.g. temperature, background pressure, reactive gas, laser fluence, ablation frequency, etc.), this makes it extremely complex and introduces an intricate web of interdependencies between growth parameters.

2.3.1 | Instrumentation

The tool consists of a vacuum chamber equipped with a heatable substrate holder, a mobile target stage and gas inlets. An optical window connects an external laser setup to the vacuum chamber, allowing for the laser pulses to reach the target. To monitor thin-film evolution in real time, a Reflection High-Energy Electron Diffraction (RHEED) system is integrated into the chamber as a complementary in-situ diagnostic tool. A schematic of the experimental setup can be seen in Figure 2.8.

The high intensity laser light is focused and guided through an enclosed external optical setup, comprising mirrors, lenses, attenuators and apertures that provide control over the fluence and pulse size and shape. Multiple laser parameters can be adjusted, such as pulse length, frequency, and fluence, directly impacting the ablation process and consequently the film growth. All the other components are separately enclosed in a vacuum chamber (Figure 2.8) endowed with pumps, ensuring minimal contamination and pressure standarization. Dedicated gas inlets are present for the introduction of reactive and inert gases. Furthermore, both the target and substrate holder allow for z-movement motion, necessary to set a precise target-substrate (T-S) distance during growth. The target holder also allows for horizontal x-y motion, needed during patterned

ablation. Finally, the integrated RHEED system specifically comprises an electron gun and a photoluminescent detector screen positioned on opposing sides of the chamber.

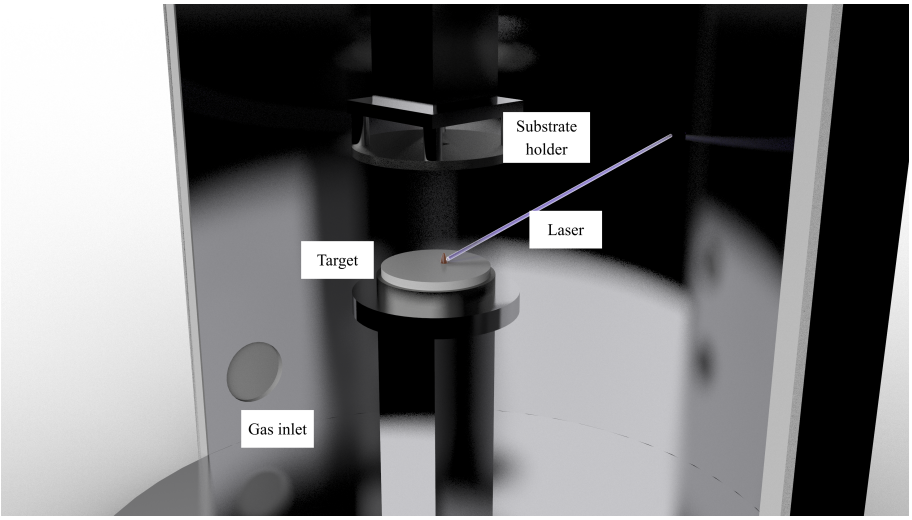

Figure 2.8: Illustrative schematic of the Pulsed Laser Deposition tool.

2.3.2 | Physical Mechanisms

Three main physical mechanisms are worth further discussion: laser ablation, plasma formation and expansion and nucleation on the substrate.

The first stage, laser ablation, starts the moment the laser strikes the target. During this process, a fraction of the target material is removed, resulting in the formation of a dense gaseous vapour layer localized directly above the target surface [35]. Crucially, effective ablation requires that the material absorbs the specific wavelength of the incident laser [41]. A combination of electronic excitations caused by photon absorption and thermal and non-thermal processes contributes to this phenomenon [41].

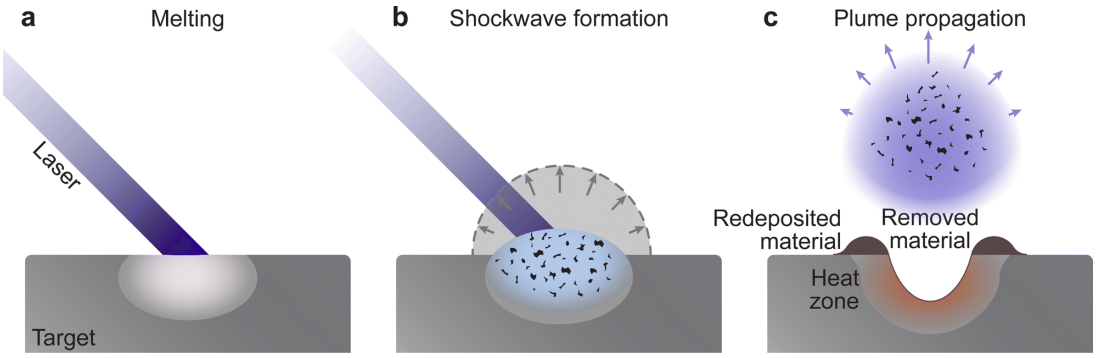

Figure 2.9: Physical mechanisms of PLD. Ablation, vaporisation, and expansion [41].

The laser and material interaction is driven by the excitation of electrons by an incoming photon [14, 41]. The absorption of a photon promotes the electronic transition of an electron from the ground state to an excited state. Shortly thereafter, these excited electrons undergo relaxation through electron-phonon coupling [41]. As the rapid electron excitation occurs, the material is brought to extreme high temperature within a matter of nanoseconds [41]. Once the system relaxes, this thermal energy is transferred to the system, inducing the melt and evaporation of

the ablated area [14], which ultimately forms the initial vapour layer. The process will only induce a stoichiometric ablation if non-thermal processes dominate. This is that at fluences above a certain threshold, congruent ablation occurs [55], and further photoexcitation leads to non-thermal ejection from the material. For fluence values below the specific threshold and in the case that thermal processes dominate, a non-stoichiometric plasma plume would be created due to the differences in melting temperatures and evaporation pressures [14, 35]. As previously noted, both processes coexist during ablation but their relative dominance dictates the final film stoichiometry.

Concurrently, laser absorption by the solid target is also accompanied by photon absorption within the emerging vapour layer. In this region, absorption happens via two main processes: photoionization and inverse Bremsstrahlung [41, 36]. During photoionization, atoms absorb incident photons with sufficient energy to eject bound electrons. Complementary, electrons can gain enough kinetic energy to be ejected by the transfer of energy due to neighbouring collisions [41]. This cascade of collisions increases the density of the vapour layer and establishes a localised region known as the Knudsen layer, which acts as the primary driver for plasma expansion [41, 14].

The initial phase of plume expansion is highly collisional, ultimately defining the level of ionization of the plasma plume [41]. Following this one-dimensional expansion, the plume undergoes an adiabatic expansion characterized by particle-free motion when expanding in vacuum [36]. However, in the presence of a background gas, this free expansion regime is truncated as the plume pressure drops and becomes comparable to the ambient pressure [36]. Although further discussion of the influence of a background gas will follow in the next section, it is worth mentioning here that the plume slows down in the presence of background pressure. This effect forms a shock-wave at the plume-gas interface, directly regulating the kinetic energy of the plasma [41, 36]. At the same time, spatial and mass separation occur within the plume itself; ion charges separate and accelerate depending on their mass. Light elements and electrons guide the plume, followed by the heavy particles. This distribution leads to the formation of an electrostatic gradient which, in turn, accelerates the ions inside the plume [41].

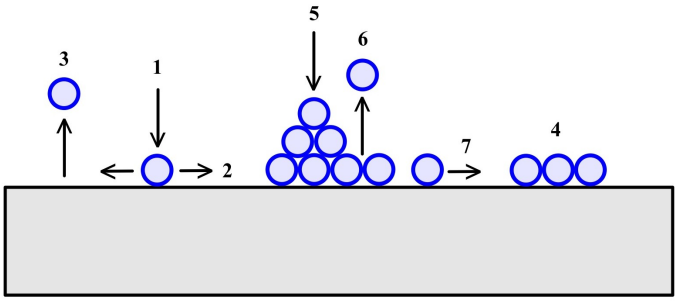

Figure 2.10: Possible paths for adatoms during the deposition process: 1-adsorption, 2-surface diffusion, 3-desorption, 4-cluster nucleation, 5-adsorption on island, 6-desorption from island, 7-dissociation from a cluster. Inspired by [54].

Growth commences once the plume reaches the surface of the substrate. The arriving species can take different paths: adsorption, diffusion, desorption, nucleation, incorporation or dissociation (Figure 2.10) [54]. The dominance of any of these processes depends heavily on growth

conditions, including substrate, laser properties such as fluence, frequency or spot size, growth temperature or background pressure, among many others [10]. Ideally, plume atoms adsorb onto the substrate surface, carrying enough kinetic energy to diffuse and incorporate at the appropriate spot in the lattice [36].

2.3.3 | Influence of Growth Parameters

In this work, the background pressure and substrate temperature are systematically varied, directly impacting the growth rate, crystal quality and surface morphology of the film. It is important to understand that, even though all other parameters are fixed, they are all interconnected in the growth process. Therefore, it is necessary to recognize the effects of each parameter on the material deposition. The influence of these on the final product manifests in two different ways: the modification of plume dynamics or the alteration of surface kinetics.

The physics of plume dynamics are intrinsically tied to the interplay between the plume and the ambient environment. Introducing a background gas directly slows down the plasma, as the kinetic energies of the in-flight species are affected [14, 41]. Simultaneously, the background gas influences the compositional incorporation, crystallinity and growth rate of the film [14, 41]. Inert gases, such as Argon (Ar), are primarily introduced to control the kinetic energies of the ablated species without chemically reacting with them, making them highly valuable for fundamental kinetic studies [41]. Conversely, reactive gases, such as O_2, allow for the incorporation of volatile elements to compensate for potential stoichiometric deficiencies in the plume [41]. For the growth of oxides -in the context of this work- excess oxygen is necessary to increase the growth rate, as it favours the thermodynamics of Ga_2O_3 formation (Equation (2.4)). At high pressures, collision frequency increases, leading to the formation of ionic clusters before reaching the substrate. Once they incorporate, these clusters coalesce into distinct grains and act as nuclei seeds [14]. Consequently, films grown at pressures higher than 10^{-2} mbar usually present higher compositional and thickness homogeneity and grainy-like surfaces [41, 14]. On the other hand, under relatively low ambient pressures ($<10^{-3}$ mbar), the kinetic energy of the arriving species is still noticeably large. This leads to velocity disparities of the plume components, affecting the arrival times to the substrate directly and, as a result, the growth of the film [41]. Because kinetic energy attenuation is minimal in this low-pressure regime, the ablated species arrive predominantly as individual atomic or molecular species [14]. Furthermore, the risk of re-sputtering, in particular of lighter elements, of elements from the thin-film surface increases due to the high kinetic impact of the plasma [41].

Beyond background pressure, plume dynamics are also influenced by three other variables: laser fluence, target-substrate (T-S) distance and spot size. Fluence is defined as the pulse energy delivered per area (in J/cm^2), and is a key parameter determining both the ablation rate and the composition and shape of the plume [8]. Consequently, the selected fluence may affect, as a result, the final film's surface roughness, thickness, composition, crystal quality and subsequent optical and transmittance characteristics [8, 41]. Nevertheless, a minimum fluence is needed for the congruent ablation and ejection of material: the fluence needs to exceed the binding energy of the solid target [14].

While T-S distance doesn't directly alter the plume dynamics, it can affect the ablation process and plume composition. Furthermore it determines, next to other parameters, the fraction of the plume that reaches the substrate. In simple terms: shorter T-S distances can induce the

re-sputtering of arriving species (at high chamber pressures) due to excessive kinetic impact, whereas large distances attenuate the deposition rate, leading to lower material transfer [41, 14]. Therefore, finding an optimal distance is required. Finally, the laser spot size on the target determines the amount of material removed per pulse and sets the opening angle of the plume. This angle follows an inverse relationship, where smaller spots create a wider dispersion angle and vice versa [41]. As a result, using smaller laser spot sizes generally yields a more consistent thickness distribution across the film surface [54].

In order to promote the surface diffusion of adatoms, the substrate is typically heated during deposition. This thermal activation provides sufficient energy to improve adatom mobility, which in turn enhances surface diffusion into energetically favourable sites [14, 41]. As a result, generally, this enables the growth of higher quality crystalline films, compared to those deposited at lower temperatures. Simultaneously, high temperatures boost island coalescence and allow surface impurities to desorb more easily [41]. Beyond a critical material-dependent temperature, crystalline quality worsens due to re-evaporation and desorption, and growth rate decreases.

2.4 | Characterization

To assess the quality of the grown layer, two main characteristics have been studied: crystallinity and growth rate. The layer is studied visually and topographically, as well, to observe surface roughness, domain sizes and/or defects.

2.4.1 | Spectroscopic Ellipsometry

Ellipsometry is an optical measurement technique used to characterize the change in light polarization upon reflection from a sample [37, 7]. Because of its non-destructive and non-invasive nature, ellipsometry is a great tool for thin film studies [32].

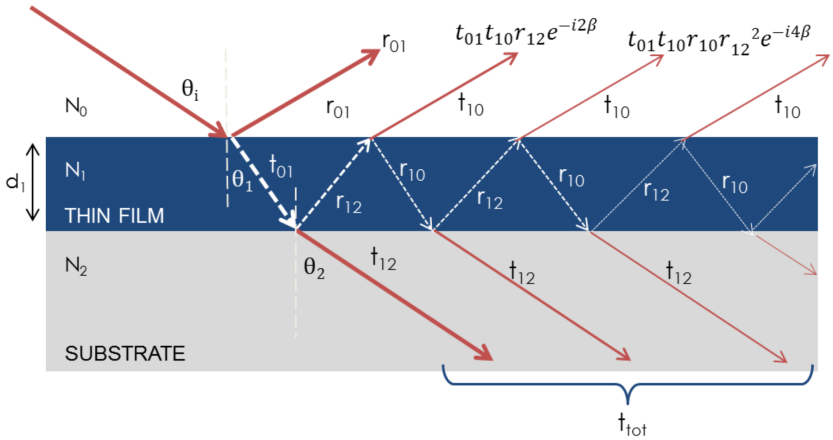

Figure 2.11: Light interaction with sample interface, where *t* components represent transmission coefficients [19].

An ellipsometry tool consists of a white light source, a polarizer generator, a polarizator analyzer and a light detector, which are used to measure a sample. Two polarization directions are defined along the plane of incidence: p-polarization (parallel to the plane of incidence) and s-polarization

(perpendicular to the plane of incidence). The reflection coefficients of each of these polarization components (r_p, r_s) can be described by:

$$r_p = \frac{(n_s + ik_s) \cdot \cos\phi_0 - n_0 \cdot \cos\phi_s}{(n_s + ik_s) \cdot \cos\phi_0 + n_0 \cdot \cos\phi_s} \qquad r_s = \frac{n_0 \cdot \cos\phi_0 - (n_s + ik_s) \cdot \cos\phi_s}{n_0 \cdot \cos\phi_0 + (n_s + ik_s) \cdot \cos\phi_s}$$

Here n is the refractive index and k is the extiction coefficient. Both parameters are material-dependent. The angles can be determined from Snell's law [32]. As these components interact with the sample, both phase and amplitude of the incident light change. The change in polarization after optical interaction with the sample can be mathematically derived through the complex ratio of Fresnel reflection coefficients:

$$\rho = \tan\Psi \exp^{i\Delta} = \frac{r_p}{r_s} \tag{2.9}$$

where Ψ and Δ represent the amplitude ratio and the phase difference, respectively. These two parameters are the raw quantities derived by the tool.

For multilayer films, which are treated in this work, film thickness can be related to the so-called phase thickness β, a parameter that accounts for the total delay the light experiences after total interaction between light and film, by:

$$\beta = 2\pi \left(\frac{d}{\lambda}\right) n_1 \cos\theta_1$$

In order to properly derive the parameters of interest, a specific model must be fitted for the measured sample. In this case, two dispersion models have been employed: Lorentz and Cauchy. The latter serves as a good fit for Ga_2O_3 films on sapphire, and allows for simplicity and fit ease. It follows as

$$n(\lambda) = A + \frac{B}{\lambda^2} + \frac{C}{\lambda^4}$$

where A, B and C are fitting parameters and λ is the light wavelength.
For β-Ga_2O_3 on GaN/Al_2O_3 a Cauchy, together with a Lorentz approach, has been used [38, 59]. The reason lies in the complexity of the multilayer system. The Lorentz oscillator formula is described as:

$$\epsilon(w) = 1 + \frac{(\epsilon_s - 1)\omega_t^2}{\omega_t^2 - \omega^2 + i\Gamma_0\omega} = \epsilon_1(\omega) + \epsilon_2(\omega)$$

where $\epsilon_1 = n^2 - k^2$ and $\epsilon_2 = 2nk$.

Although spectroscopic ellipsometry allows for fast measurement, its analysis complexity hinders the modelling step, especially for samples with very rough surfaces. Therefore, throughout this work, data obtained with this tool are presented as an estimate for film thickness trends rather than an absolute value.

2.4.2 | X-ray Diffraction

X-ray Diffraction (XRD) is a non-destructive characterization technique for crystalline materials. Its principle lies in the formation of constructive interference upon the interaction between monochromatic X-rays and a crystal [3]. Because of the periodic atomic nature of crystals, these

act as 3-dimensional diffraction gratings, producing constructive interference only when Bragg's law is satisfied:

$$n\lambda = 2d_{hkl}\sin\theta \tag{2.10}$$

where n is an integer, λ is the characteristic wavelength of the X-rays, d_{hkl} is the spacing between the crystallographic planes, and θ is the angle of diffraction.

Practically, X-rays are generated via a cathode ray tube, filtered to achieve monochromatism, collimated to concentrate them and finally focused towards the sample [3]. The sample is centered between the generator and a detector that collects the scattered signal. To achieve an X-ray beam, electrons are produced by the thermionic emission of a filament and accelerated by applying a voltage towards a target of choice. As electrons impact and remove inner-shell electrons of the target, characteristic X-rays are produced [3]. In this case, a Cu-K_α radiation with a wavelength of 1.54 Å is used. As constructive interference appears, the detector records this data, converting it into a count signal output.

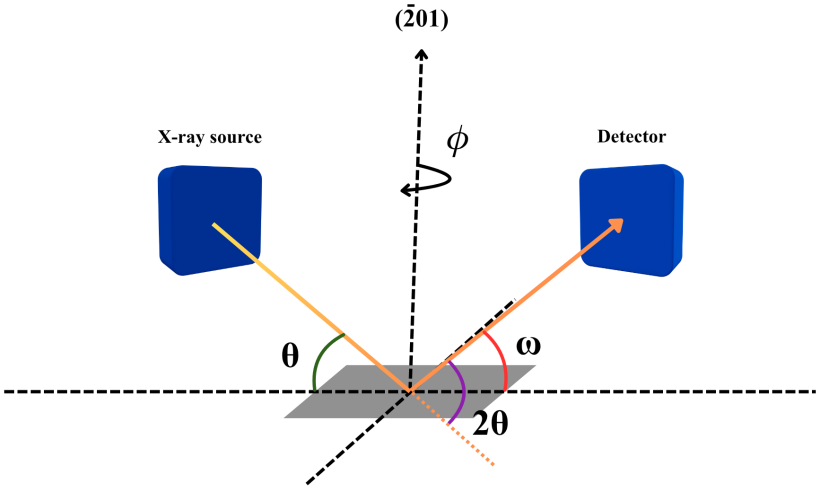

Figure 2.12: Schematic diagram of an XRD system.

The most fundamental principle of a diffractometer is the variation of two main angles: θ, which describes the angle between source and sample, and 2θ, the angle between sample and detector. More degrees of freedom can be added, such as a tilting angle ψ and a rotational angle ϕ [16]. In Figure 2.12, an illustrative schematic of the tool is shown.

XRD can be used in different modes depending on what information needs to be retrieved from the sample. Throughout this work, two main modes are explored, and are worth explaining more in depth: $2\theta/\omega$ scan and Rocking Curve (RC).

In the former, also referred to as coupled scan, the ω angle is fixed to half of the 2θ angle. During this scan, the surface plane is set in parallel to the Bragg plane (i.e. plane where Bragg's law is satisfied). Hence, this scan allows to locate the *hkl* planes that fulfil constructive diffraction only for planes parallel to the surface. Therefore, for crystal thin films, this scan permits the identification of the preferential orientation of the crystal domains and the phases present [16]. Figure 2.13 showcases the preferential orientation and characteristic family peaks of β-Ga_2O_3 on

GaN and sapphire in comparison with an amorphous film. It must be noted that the differentiation between monocrystalline and polycrystalline films can not be fully determined with this scan. Pole figures are needed to assess the overall in-plane crystallinity. These scans are usually presented in logarithmic scale; due to the nature of monocrystalline substrates, these tend to dominate, while peaks from the grown layer show with lower intensity. Epitaxially grown films usually present a set of peaks related to single crystalline orientation [16].

The Rocking Curve scan involves, as its name suggests, *rocking* the sample about the ω angle. The 2θ angle is fixed to the central angular position of the reflection of choice. Here, the not-parallel surface planes are brought into the Bragg plane [16]. The result of this scan is a single normal distribution curve, indicating the distribution of planes with respect to the tilt. The width of this curve is representative of the density of defects, substrate curvature and mosaic spread of grains [16]. Therefore, to assess the crystal quality, the Full Width Half Maximum (FWHM) of the curve is recorded. The peak is fitted with a Pseudo-Voigt fit (Equation (2.11)), with the FWHM indicating the epitaxial quality of the layer (i.e. smaller FWHM values indicate higher crystal quality).

$$y = y_0 + A\left[\mu\left(\frac{2}{\pi}\right)\left(\frac{w}{4(x-x_c)^2+w^2}\right) + (1-\mu)\left(\frac{\sqrt{4\ln 2}}{\sqrt{\pi}w}\right)\exp\left(-\frac{4\ln 2}{w^2}(x-x_c)^2\right)\right] \tag{2.11}$$

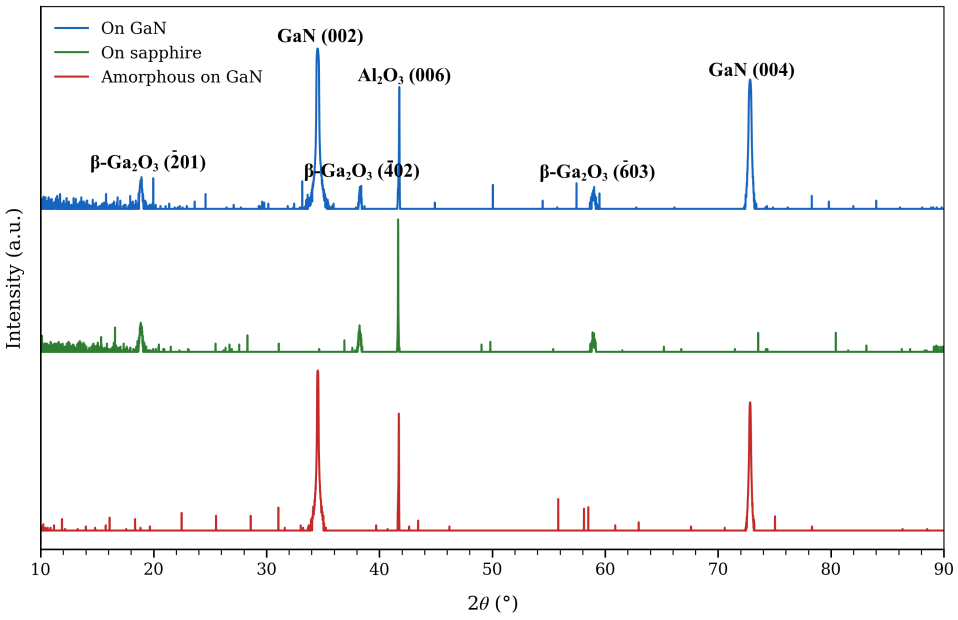

Figure 2.13: 2θ scans showing the different orders of reflection for $(\bar{2}01)$ β-Ga_2O_3 domain orientation on GaN and sapphire. An amorphous Ga_2O_3 layer on GaN is also plotted for comparative reasons.

2.4.3 | Atomic Force Microscopy

The characterization of surface topology is achieved via Atomic Force Microscopy (AFM). In this method, a sharp tip is mounted on a flexible cantilever, and it is scanned across a region of interest while the deflection of the cantilever is recorded with the aid of a laser and a photodetector. The measured forces between tip and sample are usually classified by their contribution range and

strength. These can be van der Waals, magnetic or chemical forces, among others [13].

The cantilever experiences a topology-dependent bending and reflects the height changes of the specimen. This bending simply follows Hooke's law, describing the normal force between tip and sample:

$$F = -k\Delta z$$

Here, k is the spring constant of the cantilever, and Δz is the experienced bending in nm. As the cantilever bends while scanning the sample, a laser diode is pointed at the cantilever. The reflection of the beam is refocused onto a photodiode, which records the movements of the reflected laser beam depending on the bending of the cantilever.

The tip experiences a non-linear force that changes with the tip-sample separation [34]. Therefore, two different regimes can be distinguished according to the behaviour of force versus tip-sample distance: repulsive and attractive. The AFM can be operated in three different modes: contact, intermittent and non-contact. This can be observed in Figure 2.14.

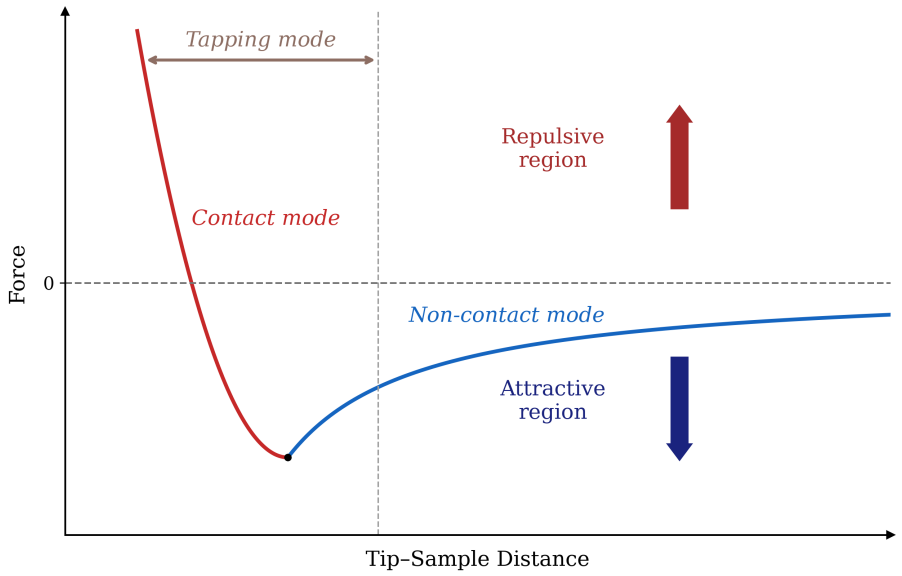

Figure 2.14: Force behaviour with respect to tip-sample distance.

In the first mode, the tip is located close to the sample, in the repulsive region of the plot. Here, the vertical deflection of the cantilever (i.e. force) is maintained constant during the scan by a feedback circuit that monitors the photodetector signal [34]. This regime is referred to as contact mode, as the probe remains in contact with the sample throughout the scan. While effective for imaging hard, somewhat flat surfaces [52], lateral forces may damage the tip or the sample [20, 47]. Furthermore, forces higher than a few nN can cause deformation, leading to poor image resolution and feature damage [20, 47].

To avoid these drawbacks, intermittent (or tapping) mode was utilized throughout this work. Here, a piezoelectric component oscillates the cantilever near its resonance frequency (i.e. frequency with maximum amplitude) [47]. As the tip scans the surface, it *taps* the sample at the bottom of each oscillation cycle [34]. Surface features alter the oscillation amplitude of the cantilever, which is reflected in the laser's position on the photodiode. Because this mode provides zero

lateral force, it is great for soft or fragile samples as it provides general good imaging and is less prone to sample damage and tip wear [47].

Alternatively, in non-contact mode, the tip is positioned far away from the specimen. Hence, long-range interactions, such as van der Waals forces, dominate between probe and sample. The cantilever amplitude is noticeably smaller than for the tapping mode [20]. Instead of tracking the amplitude differences due to physical contact, the cantilever's resonance frequency or phase is monitored. Although the use of this mode eliminates possible tip-sample damage and provides, in theory, high-resolution, it is highly sensitive to surface fluid layers and typically requires ultra-high vacuum conditions for efficient operation [20].

Because the system is equipped with a feedback loop, a constant force is ensured. Therefore, AFM primarily measures the height of the studied sample. The data obtained is transferred to an analysis software (e.g., Gwyddion) for post-processing and data analysis. The data is treated with two main corrections to ensure accuracy: polynomial background removal and polynomial row alignment. These steps are critical to eliminate inherent instrumental artefacts, such as sample tilt or line-to-line height shifts, which would otherwise distort the measurements. After the image post-treatment, a statistical analysis is performed to determine the root-mean-square (RMS) surface roughness.

2.4.4 | Scanning Electron Microscopy

Scanning Electron Microscopy (SEM) is a characterization technique used to examine and analyse microstructure morphologies. Here, a focused electron beam is scanned across a surface, producing high-resolution images from the emitted signal upon interaction with the sample. SEM is a great tool to understand the surface morphology over a large area in a fast manner, and it serves as a complementary technique to AFM.

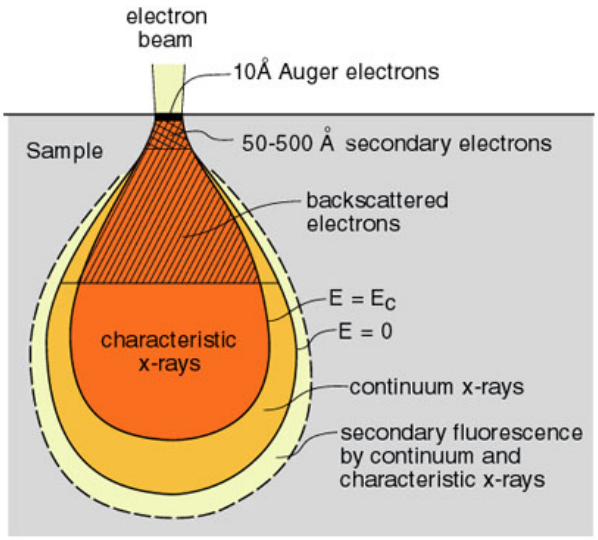

Figure 2.15: SEM interaction volume and emitted depth-dependent signals [45].

Image acquisition is based upon the interaction of an electron beam with a sample. Electrons lose energy due to the scattering and absorption processes occurring during interaction with the specimen's volume. The size of the interaction volume (Figure 2.15) is material and elec-

tron beam-dependent [26]. The interactions can be categorized into two: elastic and inelastic [61].

The former is characterized by negligible energetic losses upon interaction. The incident electron just deflects, changing its initial direction [61]. This signal is referred to as backscattered electrons (BSE) and it provides both compositional and topographic information [26]. The number of emitted BSE directly depends on the atomic number of the specimen (higher number, more BSE), and the employed accelerating voltage of the beam [61].

On the other hand, inelastic scattering occurs as the beam electrons interact and transfer substantial energy to the specimen's atoms. This transfer allows for the emission of secondary electrons (SE). Depending on the depth achieved by the incident electron through the sample, a variety of signals are produced. These include SE, Auger electrons, characteristic X-rays, and Bremsstrahlung X-rays. Here, we may focus on SE. Due to their low energy (typically 3–5 kV), secondary electrons can only escape from the shallow surface layer (a few nanometers deep) of the material [61]. Therefore, this type of signal is typically used to obtain a good topographic contrast [61], allowing for a detailed visualization of the surface morphology.

To collect the emitted electrons, different detectors are employed. These depend on the type of signal and also on the elements one is interested in imaging. In the context of this work, the so-called in-lens detector has been used. This detector primarily recovers vertically ejected SE and is positioned, as its name suggests, above the objective lens [9]. Because the collected electrons arise directly from the near-surrounding of the electron beam-sample interaction, this detector provides the highest spatial resolution information [24]. Other detectors, such as SE2, backscattered or transmitted electron detectors, can also be found in a SEM, although they won't be discussed here.

3 | Methodology

β-Ga_2O_3 layers are deposited, as introduced in Section 2.2.5, onto 1x1 cm (0001) sapphire and (0001) GaN templates on sapphire. The GaN templates were deposited by metal-organic chemical vapour deposition (MOCVD) on (0001) sapphire (RISE ProNano). The PLD target consisted of sintered Ga_2O_3 with a purity of 99.999%. Prior to growth, the substrates were sequentially ultrasonicated in Remover 1165 (organic solvent), isopropanol, acetone and deionized water for 5 minutes each, followed by drying with a N_2 gun to remove any residual contaminants.

The PLD tool, from TSST, uses a 248 nm KrF laser with a fixed fluence of 27.7 mJ and energy density of 1.5 J/cm^2. The number of pulses is set to 5000, unless otherwise stated, with a pulse frequency of 2 Hz. The pulse has a rectangular shape with size 1.99x0.90 mm. The distance between the target and the substrate is kept at 55 mm.

The growth experiment is initiated by introducing the target and the substrate inside the vacuum chamber. After, the O_2 pressure is stabilized and the heating is ramped up until the intended temperature is reached. Before the growth starts, the target, which has been mechanically polished with a P320 sandpaper, is pre-ablated inside of the chamber to ensure a smooth and flat surface before deposition. During this process, the substrate is physically protected by a shutter.

The parameters used in each growth can be found in Table 3.1. It is important to notice that the baseline vacuum chamber pressure is 10^{-6} mbar. This does not indicate there is an oxygen influx. Two series of samples on sapphire and GaN-on-sapphire templates are grown.

Table 3.1: Growth parameters of epilayers on GaN and sapphire.

Film	Temperature (°C)	Pressure (mbar)
L1	750	10^{-6}
L2	700	10^{-6}
L3	600	10^{-6}
L4	800	10^{-5}
L5	750	10^{-5}
L6	700	10^{-5}
L7	600	10^{-5}
L8	550	10^{-5}
L9	500	10^{-5}
L10	750	10^{-4}
L11	700	10^{-4}
L12	600	10^{-4}
L13	800	10^{-2}
L14	750	10^{-2}
L15	700	10^{-2}
L16	600	10^{-2}
L17	750	10^{-1}

Characterization of the grown samples is carried with Woolam RC2 Ellipsometer, Bruker AFM Icon, Bruker D8 Discover XRD and Zeiss Gemini SEM. For more details on tool specifications, please refer to Appendix A.

4 | Results & Discussion

This section describes the results of β-Ga_2O_3 growth on GaN templates and sapphire substrates as a function of oxygen pressure and growth temperature. The crystalline quality of the films is assessed using the FWHM of the β-Ga_2O_3 ($\bar{2}01$) diffraction peak. Film thickness is determined by spectroscopic ellipsometry and subsequently used to calculate growth rates. In addition, the influence of growth temperature on surface roughness is systematically investigated.

4.1 | Growth behaviour of β-Ga_2O_3

4.1.1 | Growth rate

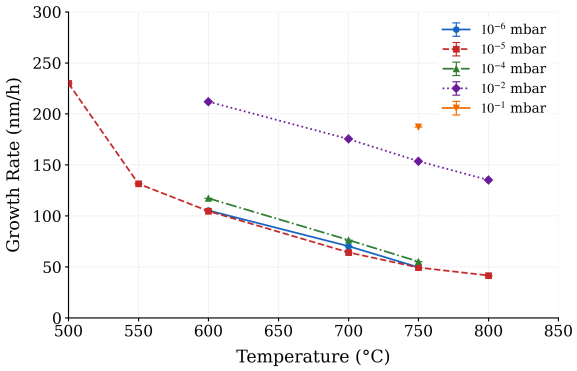

(a) Growth rate as a function of temperature on GaN.

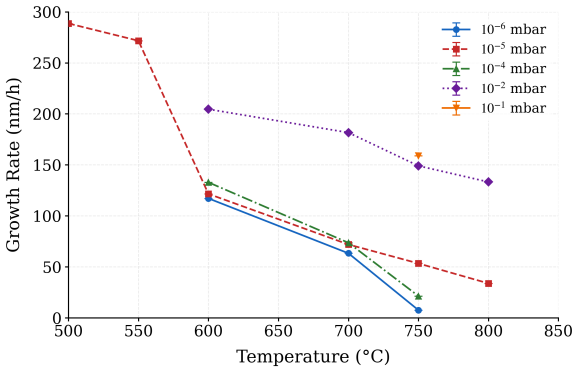

(b) Growth rate as a function of temperature on Al_2O_3.

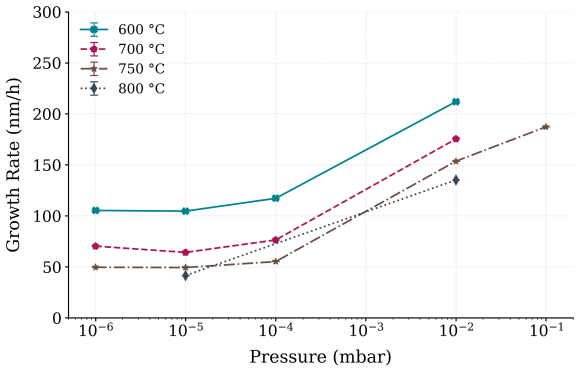

(c) Growth rate as a function of pressure on GaN.

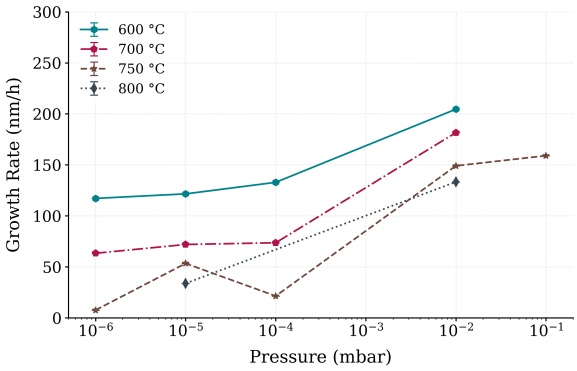

(d) Growth rate as a function of pressure on Al_2O_3.

Figure 4.1: Growth rate in nm/h as a function of variable growth parameters.

Figure 4.1 shows the dependence of growth rate on temperature and oxygen pressure for films grown on GaN templates and sapphire substrates. At a fixed oxygen pressure, the growth rate decreases with increasing substrate temperature for both substrate types, indicating an inverse relationship between these parameters (Figure 4.1a and 4.1b). This trend highlights the increasing influence of thermal desorption kinetics at elevated temperatures. As the substrate temperature increases, the desorption rate of Ga-containing species rises, reducing their residence time on the growth surface and consequently lowering the probability of complete oxidation and formation

of Ga_2O_3.

The same behaviour may also be interpreted from a thermodynamic perspective, whereby Equation (2.4) increasingly proceeds in the reverse direction at higher temperatures. Under these conditions, Ga_2O_3 becomes less stable and its decomposition into volatile $Ga_2O_{(g)}$ and $O_{2(g)}$ is promoted. The formation and re-evaporation of gallium suboxide species is known to play an important role in several physical vapour deposition techniques [53, 51, 12]. Consequently, stable incorporation of Ga_2O_3 directly competes with the formation and desorption of volatile gallium suboxide species.

Lowering the temperature down to 500°C and for an oxygen pressure of 10^{-5} mbar, a pronounced increase in growth rate is observed for films grown on both GaN templates and sapphire substrates (Figure 4.1a and 4.1b). These conditions lead to the formation of amorphous Ga_2O_3 as deduced from XRD (see Figure 2.13). At such low temperatures, the thermal energy available to adatoms is limited. Furthermore, the increased sticking coefficient results in a higher net growth rate. Together, these effects reduce the effective surface diffusion length, preventing adatoms from reaching energetically favourable lattice sites prior to incorporation. Instead, species become incorporated into a disordered amorphous matrix. Since amorphous growth is not constrained by the nucleation and lattice-site requirements of crystalline growth, significantly higher sticking coefficients and growth rates can be achieved. This is the reason why the growth of amorphous Ga_2O_3 is observed at very high growth rates.

The influence of oxygen pressure on growth rate is shown in Figure 4.1c and 4.1d. For both substrate types, at constant temperature, the growth rate generally increases with increasing oxygen pressure. Higher oxygen pressures promote more efficient oxidation of Ga-containing species and increase the fraction of ablated material that is successfully incorporated into the growing Ga_2O_3 film. From a kinetic perspective, oxygen-rich environments enhance the sticking coefficient of Ga-containing species while simultaneously suppressing desorption.

Within the oxygen-pressure range of 10^{-6} mbar to 10^{-4} mbar, the growth rate exhibits a distinct plateau for all investigated temperatures on both GaN templates and sapphire substrates, indicating only a weak dependence on oxygen pressure in this oxygen-poor regime. Note that the growth at 750°C and 10^{-4} mbar appears as an outlier. This deviation may be related to pressure fluctuations during the deposition, as these pressures are close to the lower operating limit of the mass-flow controller. Overall, the trends confirm the expectation that, under oxygen-poor conditions, lower substrate temperatures are required to suppress Ga_2O_3 decomposition and maintain a reasonable growth rate.

4.1.2 | Structural quality

4.1.2.1 | On sapphire

Figure 4.2 summarizes the growth parameter space explored on sapphire substrates, showing the substrate temperature and oxygen pressure conditions together with the corresponding FWHM values of the $(\bar{2}01)$ rocking curve of each crystalline film.

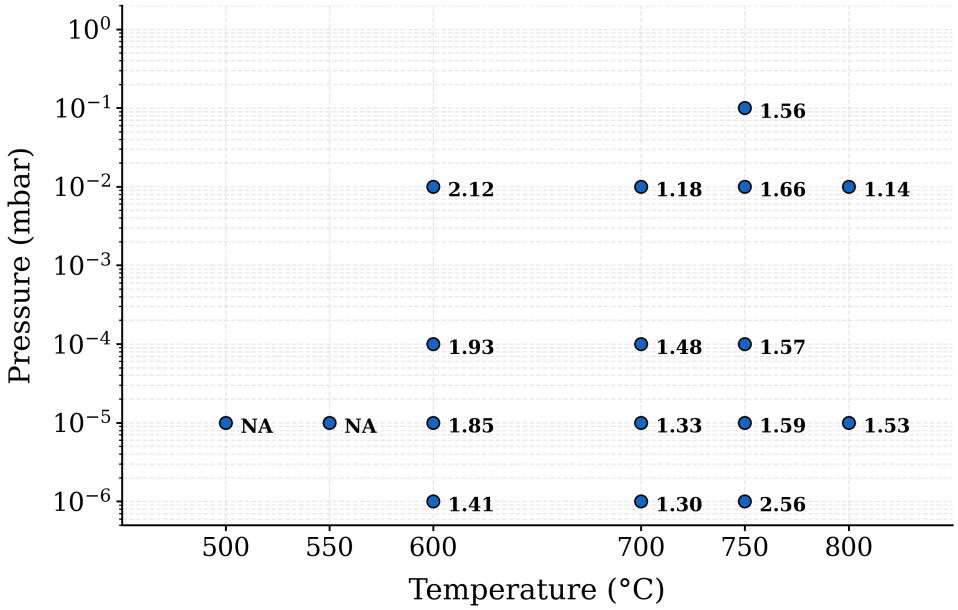

Figure 4.2: FWHM (°) values for the ($\bar{2}01$) rocking curves are indicated for samples grown on sapphire. NA corresponds to amorphous films.

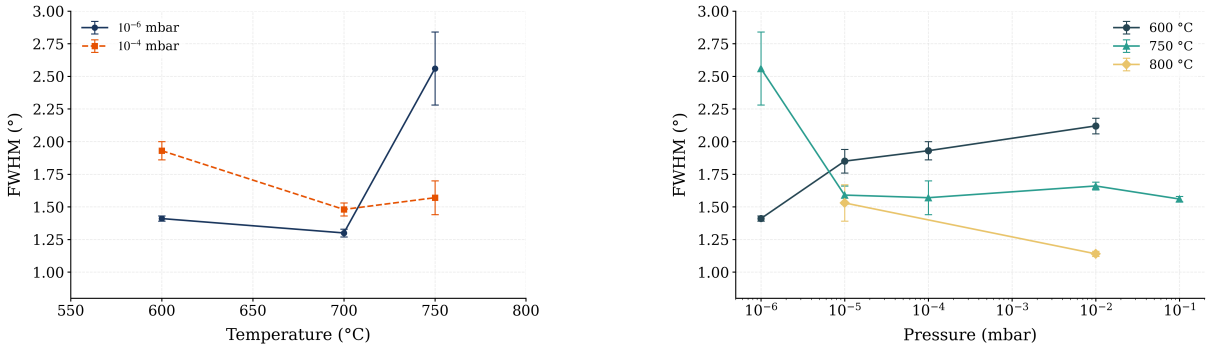

(a) **(b)**

Figure 4.3: (a) Temperature and (b) pressure dependencies of FWHM on sapphire.

The crystallinity of the β-Ga_2O_3 films on sapphire exhibits an interesting dependence on both growth temperature and oxygen pressure. Figure 4.3a shows the FWHM of the ($\bar{2}01$) rocking curve for films grown at oxygen pressures of 10^{-4} mbar and 10^{-6} mbar as a function of growth temperature. At 10^{-6} mbar (background pressure), no additional oxygen is supplied to the chamber beyond that originating from the ablated target material. At 600°C, sufficient oxygen from the target is available to enable the growth of stoichiometric and crystalline β-Ga_2O_3, yielding a rocking-curve FWHM of 1.41° at a growth rate of approximately 117 nm/h. Increasing the growth temperature to 700°C reduces the FWHM to 1.30°, indicating improved crystallinity. This behaviour is consistent with the increase in adatom surface mobility expected at higher temperatures within the incorporation-limited growth regime, as discussed in Section 2.2.3.

At 10^{-6} mbar, a further increase in temperature to 750°C leads to a significant deterioration in crystallinity, with the FWHM increasing to 2.56°. At this temperature, the system appears to enter a desorption-dominated regime, in which the residence time of Ga-containing species on the growth surface becomes insufficient for efficient incorporation into the crystal lattice. The

surface diffusion length is considerably small. As a result, crystalline growth is hindered and the film quality deteriorates. A similar trend is observed at an oxygen pressure of 10^{-4} mbar. However, the degradation in crystallinity at 750°C is less severe than that observed at 10^{-6} mbar. This may be related to the enhanced oxygen availability at 10^{-4} mbar which suppressed thermal decomposition and promotes the incorporation of Ga-containing species.

Figure 4.3b shows the FWHM of the $(\bar{2}01)$ rocking curve for films grown at 600°C, 750°C and 800°C, as a function of growth pressure. At 600°C, the crystallinity deteriorates as oxygen pressure increases. Under these relatively low-temperature conditions, higher oxygen pressures favour the thermodynamics of Ga_2O_3 growth, resulting in higher growth rates. Combined with the limited thermal energy available to adatoms, this reduces the effective surface diffusion length prior to incorporation, making it more difficult for species to reach energetically favourable lattice sites. Consequently, the FWHM increases with oxygen pressure, indicating poorer crystallinity.

The opposite trend is observed at higher growth temperatures (750°C and 800°C), where the FWHM decreases with increasing oxygen pressure. At these temperatures, adatom mobility is sufficiently high that the enhanced oxidation and incorporation provided by higher oxygen pressures no longer hinder crystalline growth. At 750°C and an oxygen pressure of 10^{-6} mbar, the oxygen supply appears insufficient to sustain efficient incorporation of Ga-containing species into the growing crystal. Under these oxygen-poor conditions, desorption competes strongly with incorporation, resulting in a marked deterioration of crystallinity. These results suggest that, on sapphire, higher growth temperatures and elevated oxygen pressures are required to achieve high crystalline quality. As shown in Figure 4.2, the film exhibiting the highest crystalline quality (FWHM = 1.14°) was grown at 800°C and 10^{-2} mbar oxygen pressure. In contrast, growth at 500°C and 550°C resulted in amorphous films, consistent with the limited adatom mobility and short surface diffusion lengths expected at such low temperatures.

Overall, these results suggest that, on sapphire, for a given laser fluence, frequency, and T-S distance, lower oxygen pressures enable the growth of crystalline β-Ga_2O_3 at lower substrate temperatures while maintaining a crystalline quality comparable to that obtained at higher temperatures and oxygen pressures. The growth performed at 700°C and 10^{-2} mbar appears to be an exception to this general trend.

4.1.2.2 | On GaN

Figure 4.4 summarizes the matrix of growth temperatures and oxygen pressures investigated for growth on GaN templates, together with the measured FWHM values of the β-Ga_2O_3 $(\bar{2}01)$ rocking curves.

Figure 4.5a shows the dependence of the $(\bar{2}01)$ rocking-curve FWHM on oxygen pressure for films grown at 600°C and 700°C. At 600°C and an oxygen pressure of 10^{-2} mbar, a comparatively large FWHM of approximately 2.1° is observed, indicating relatively poor crystalline quality. As was also observed for growth on sapphire, this behaviour may be attributed to the high growth rate obtained under oxygen-rich conditions at relatively low temperature. The resulting short effective surface diffusion length limits the ability of adatoms to reach energetically favourable incorporation sites. In addition, oxidation of the GaN surface may contribute to the degradation of crystalline quality. Reducing the oxygen pressure to 10^{-4} and 10^{-5} mbar results in a marked improvement in crystallinity. Under these conditions, both the growth rate and the likelihood of

surface oxidation are reduced, which may contribute to the observed decrease in FWHM. For growth at background pressure (10^{-6} mbar), however, the FWHM increases again. This behaviour is observed for both temperature series (600°C and 700°C), suggesting that, unlike growth on sapphire, crystalline β-Ga_2O_3 growth on GaN is not favoured under background-pressure conditions. The deterioration in crystallinity at background pressures suggests that a minimum oxygen supply is required for high-quality β-Ga_2O_3 growth on GaN templates. This requirement appears to be less stringent for growth on sapphire, possibly due to differences in the nucleation process and interfacial chemistry between the two substrate types.

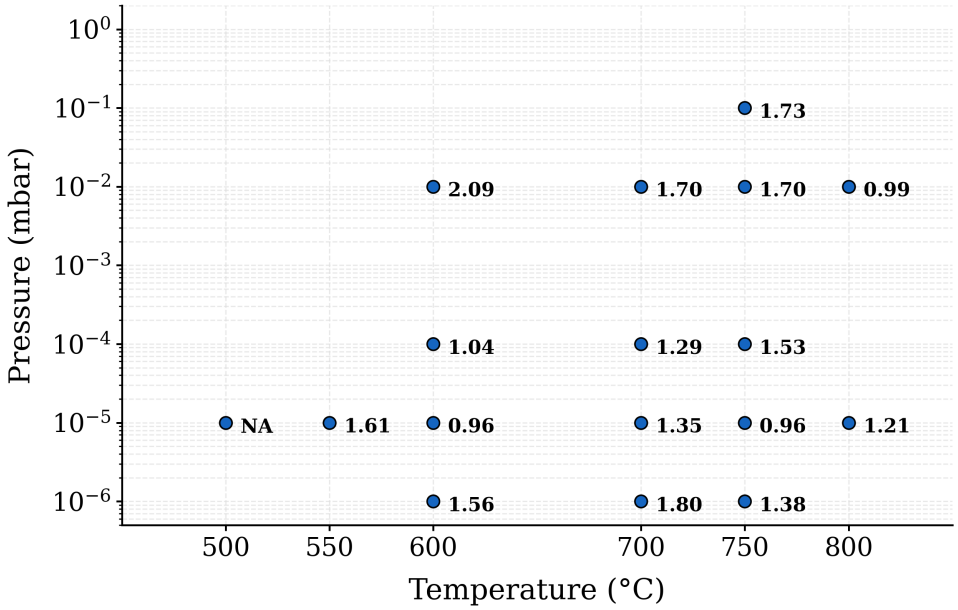

Figure 4.4: FWHM (°) values for the ($\bar{2}01$) rocking curves are indicated for samples grown on GaN. NA corresponds to amorphous samples.

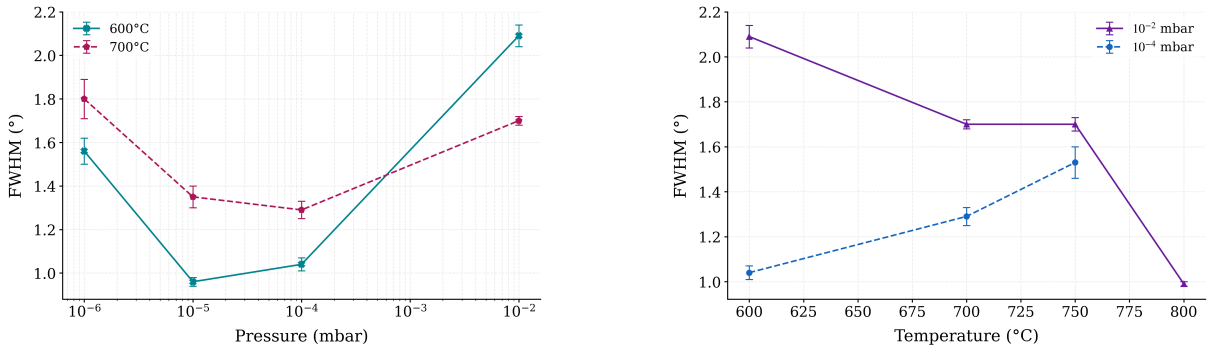

(a) **(b)**

Figure 4.5: (a) Pressure and (b) temperature dependencies of FWHM on GaN.

Figure 4.5b shows the dependence of the ($\bar{2}01$) rocking-curve FWHM on growth temperature for films grown at oxygen pressures of 10^{-2} and 10^{-4} mbar. At 10^{-2} mbar, the crystallinity improves with increasing growth temperature, as evidenced by the decreasing FWHM values. This behaviour is consistent with the increased surface mobility of adatoms at elevated temperatures, which promotes incorporation at energetically favourable lattice sites. In addition, any adverse

effects associated with oxidation of the GaN surface may be reduced at higher temperatures. The behaviour observed at 10^{-4} mbar is less straightforward. In this case, the crystallinity appears to deteriorate with increasing growth temperature, suggesting that the growth process may be approaching a desorption-dominated regime. Under these relatively oxygen-poor conditions, the increase in adatom mobility provided by higher temperature may be outweighed by enhanced desorption and reduced oxidation efficiency, leading to poorer crystalline quality. However, a similar trend is not clearly observed for films grown at lower oxygen pressures (10^{-5} and 10^{-6} mbar), where the FWHM generally decreases with temperature or exhibits greater fluctuations. The origin of this difference remains unclear and necessitates further investigation. It should also be noted that the oxygen pressure measurements were affected by a malfunctioning Pirani gauge during this period. Therefore, uncertainties in the actual chamber pressure may contribute to the observed fluctuations in FWHM and complicate the interpretation of temperature-dependent trends, particularly at low oxygen pressures below 10^{-3} mbar.

Overall, the results demonstrate that the crystalline quality of β-Ga_2O_3 grown on GaN is governed by a delicate balance between oxygen availability, surface mobility, and desorption processes. Similar to growth on sapphire, the lowest FWHM values were obtained under two distinct growth regimes: high growth temperature combined with high oxygen pressure, or lower growth temperature combined with reduced oxygen pressure. However, the deterioration in crystallinity observed at background pressure indicates that a minimum oxygen supply remains necessary for high-quality β-Ga_2O_3 growth on GaN. However, uncertainties in the oxygen pressure measurements below 10^{-3} mbar limit the precision with which these growth windows can be identified and compared. The FWHM values obtained for growth on GaN templates are generally lower than those measured for films grown on sapphire, indicating that GaN provides more favourable conditions for the heteroepitaxial growth of β-Ga_2O_3. The improved crystalline quality may be related to the smaller lattice mismatch and more favourable epitaxial relationship between β-Ga_2O_3 and GaN compared with sapphire.

4.2 | Improving crystallinity: introduction of buffer layer

To optimize the crystalline quality of the films, the primary approach is to mitigate oxidation at the substrate-film interface. To achieve this, a thin ($\sim$ 20-40 nm) buffer layer was introduced prior to the main film growth. The buffer layer was grown under identical temperature and pressure conditions as the subsequent film, but using an inert Ar background instead of O_2. Three films were grown using this two-step process under conditions corresponding to those of the films without buffer layers: Sample L14 was grown at 750°C under 10^{-2} mbar, L17 at 750°C under 10^{-1} mbar, and L13 at 800°C under 10^{-2} mbar, as compiled in Table 4.1. Each deposition consisted of 7000 pulses at 2 Hz frequency. The initial 2000 pulses were deposited under Ar gas to form the buffer layer, followed by 5000 pulses in an O_2 atmosphere to grow the main film.

This approach was motivated by the potential oxidation of GaN in an oxygen-rich ambient, as previously reported in the literature [49]. It is argued that direct exposure of the GaN template to high oxygen pressures can promote oxidation or surface modification, potentially leading to the formation of an amorphous interfacial layer that is structurally ill-suited as a template for the subsequent epitaxial growth of β-Ga_2O_3. By introducing an inert atmosphere, a controlled, low-oxygen plume arrival is ensured while reducing the chance of surface oxidation. This provides conditions closer to homoepitaxy for the successive main film growth, improving its crystallinity.

Table 4.1: RC FWHM of the tested samples with and without buffer.

Sample	Growth conditions	No buffer (°)	Buffer (°)
L14	750°C, 10^{-2} mbar	1.70	1.08
L17	750°C, 10^{-1} mbar	1.73	1.40
L13	800°C, 10^{-2} mbar	0.99	0.94

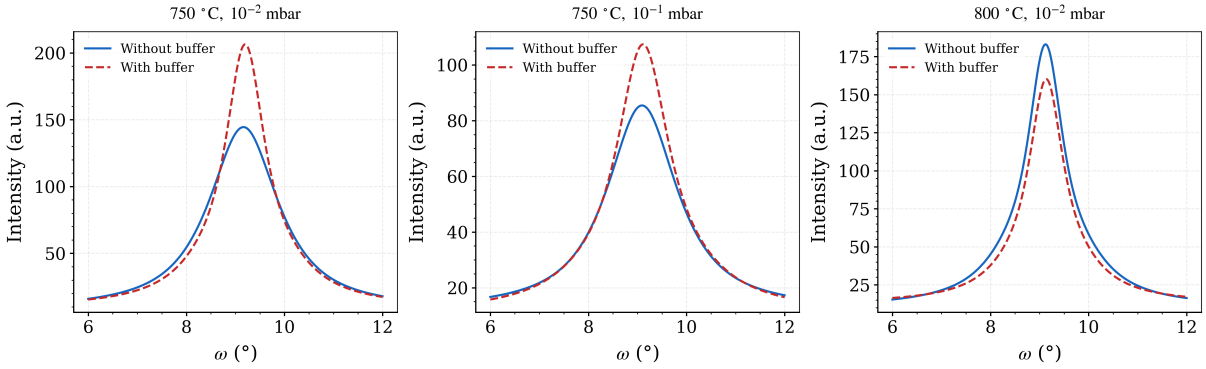

Figure 4.6: FWHM comparison of the samples grown with and without buffer layer for the samples described in Table 4.1.

As compiled in Table 4.1 and illustrated by the XRD rocking curves in Figure 4.6, the introduction of a buffer layer resulted in a consistent improvement in crystallinity across all three samples. Films grown at 750°C exhibited the most pronounced enhancements, with FWHM values decreasing from 1.70° to 1.08° and from 1.73° to 1.40°, respectively, accompanied by a substantial increase in diffraction peak intensity. Even for Sample L13, which already exhibited superior baseline crystallinity (0.99°), the implementation of the Ar buffer layer further reduced the FWHM to 0.94°. Although structural improvements were found for all samples, the magnitude of FWHM varied across the tested films. The most pronounced enhancement was observed at 10^{-2} mbar, which demonstrated an approximate 38% improvement in terms of FWHM upon implementation of the buffer.

At a growth pressure of 10^{-1} mbar, the buffer layer yields a modest 18% relative improvement in crystallinity compared to its unbuffered counterpart. This limited enhancement may be due to the high Ar background pressure (10^{-1} mbar). Because Ar does not contribute to film growth and instead scatters plasma species, it results in a thinner buffer layer. Consequently, the potential for structural improvement at this pressure is constrained, falling short of the maximum enhancement achieved at 10^{-2} mbar.

Conversely, shifting to higher temperatures at a fixed pressure of 10^{-2} mbar, the overall impact of the buffer tends to become less pronounced. High temperature increases the thermal energy of the arriving species, thereby increasing their surface diffusion lengths. This more favourable mobility allows the adatoms to efficiently hop to energetically favourable lattice sites, potentially disregarding the structural defects caused by interfacial oxidation, which is suppressed at higher temperatures. Therefore, a good crystal quality is already observed for the film grown without a buffer layer. Nonetheless, the buffer layer still provides a marginal enhancement, demonstrating that it continues to function as an oxidation-prevention transition layer.

These results provide evidence that mitigating early-stage interfacial oxidation via an inert buffer layer can be an effective approach to improving the crystalline quality of β-Ga_2O_3 on GaN templates. Particularly in conditions where thermal energy might be insufficient or in oxygen-rich environments.

4.3 | Surface morphology

The surface morphology of the β-Ga_2O_3 films was investigated using 5×5 μm^2 AFM scans to assess their surface features. In addition, the root-mean-square (RMS) roughness, which quantifies the average height variation across the surface, was used as the primary metric for morphological characterization.

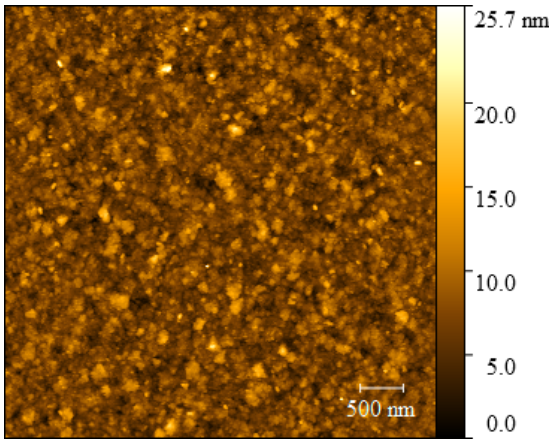

(a) β-Ga_2O_3 on GaN template with RMS roughness of 2.2 nm.

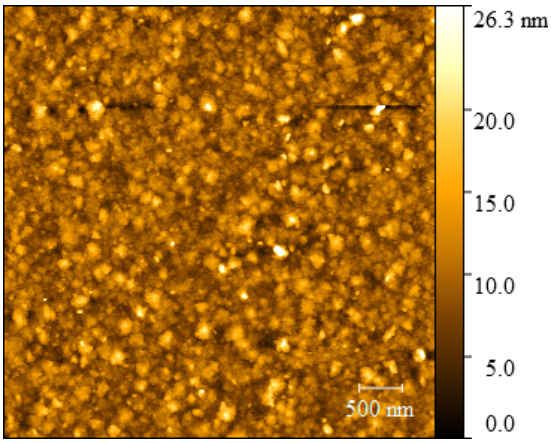

(b) β-Ga_2O_3 on sapphire with a RMS roughness of 2.9 nm.

Figure 4.7: 5x5 μm AFM images of β-Ga_2O_3 films grown at 800°C and 10^{-2} mbar on (a) GaN template and (b) sapphire.

Figure 4.7 shows the AFM images of β-Ga_2O_3 films grown under identical conditions on a GaN template and a sapphire substrate. The films display a typical columnar morphology with three-dimensional faceted grains, indicative of competitive columnar growth commonly observed in PLD-grown β-Ga_2O_3 and other oxide thin films. As shown in Figure 4.7, β-Ga_2O_3 films grown on GaN templates exhibit lower RMS roughness than those grown on sapphire under identical growth conditions. Motivated by this improved surface smoothness, a more detailed analysis of how growth conditions influence the surface morphology and RMS roughness of films grown on GaN is presented below. For completeness, morphological information about the GaN template is included. Figure 4.8 shows an SEM cross-section image and an AFM image of a representative GaN template. The GaN template exhibits a smooth step-flow surface morphology, typical for high-quality epitaxial GaN layers on sapphire substrates.

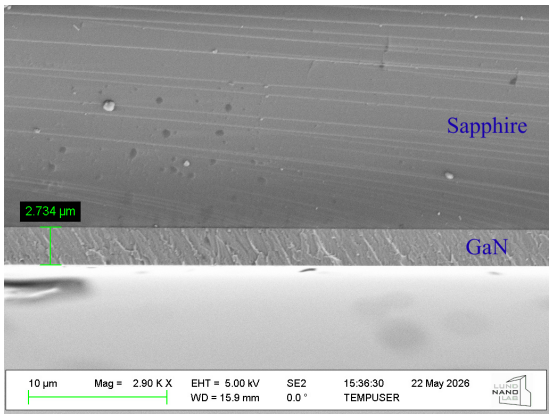

(a) SEM cross section of GaN/sapphire with an observable GaN thickness of about 2.7 μm.

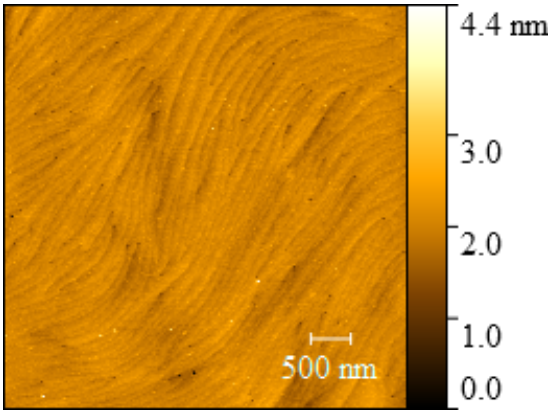

(b) 5x5 μm AFM scan of GaN surface. RMS roughness is 0.15 nm.

Figure 4.8: Morphological characterization of the utilized GaN-on-sapphire templates.

Figure 4.9 shows the RMS roughness dependence on temperature for films grown on GaN templates at fixed pressures. In general, an inverse relation between temperature and RMS roughness is found, for which RMS roughness increases with decreasing temperature. At a fixed pressure of 10^{-2} mbar, however, a distinct non-monotonic behaviour is found.

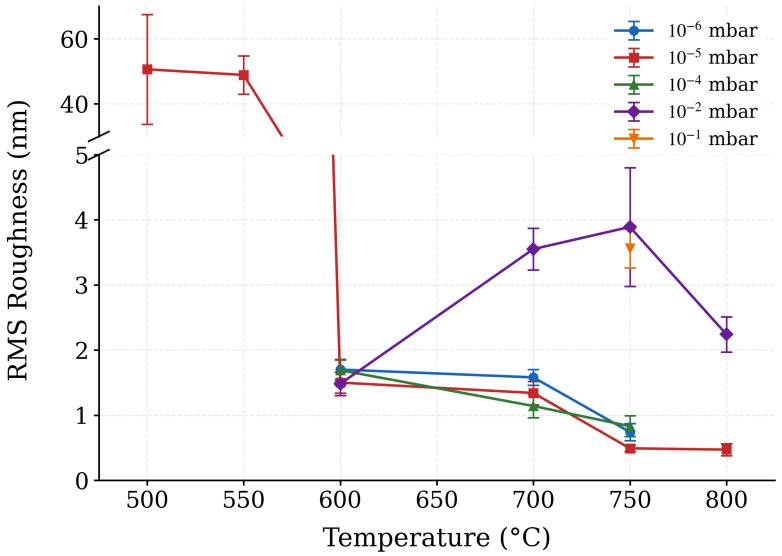

Figure 4.9: RMS trends for different pressures at varying temperatures.

For samples grown at pressures below 10^{-2} mbar, a consistent trend is observed. Decreasing substrate temperature leads to increasing RMS roughness. However, the smoothing effect typically observed at higher temperatures is less pronounced in this pressure regime. Since the growth rate decreases as oxygen pressure decreases, adatoms are expected to have a longer average surface diffusion time before incorporation. Consequently, the surface diffusion length may be larger than for films grown at higher pressures, even at the same growth temperature. This phenomenon may offer an explanation for why a similar smoothing effect is not observed once oxygen pressure is reduced.

For the set of films grown at 10^{-5} mbar, it is interesting to notice that at even lower temperatures (< 600°C), the RMS roughness increases by approximately a factor of 30, compared to the other

samples, reaching 48.9 nm and 50.6 nm for temperatures 550°C and 500°C, respectively. In this regime, the growth mode is expected to transition to three-dimensional Volmer-Weber growth, resulting in substantially rougher films (Figure 4.10).

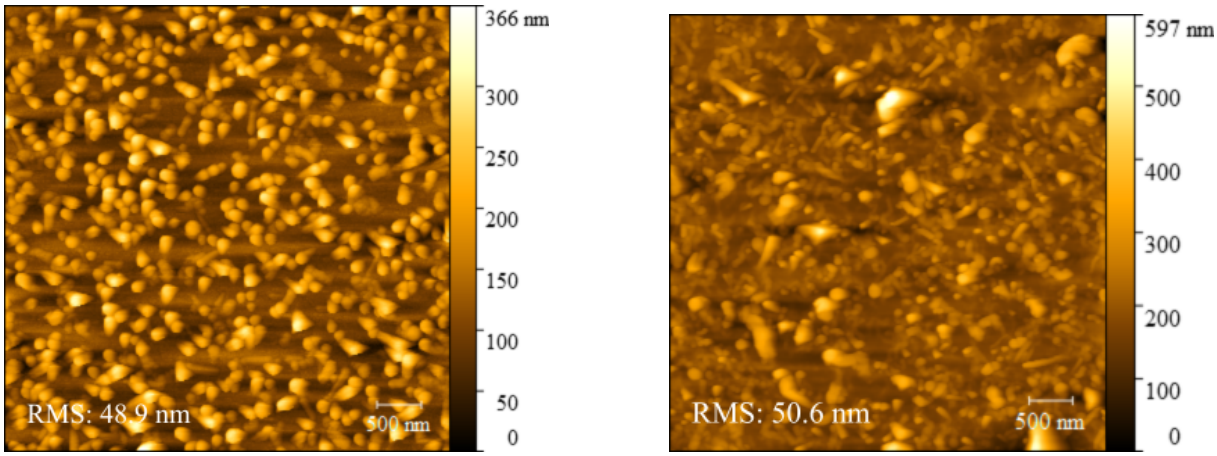

(a) **(b)**

Figure 4.10: 5x5 μm AFM scans of (a) 550°C and (b) 500°C grown films at 10^{-5} mbar.

At higher pressures (i.e. higher than 10^{-3} mbar), a general increase of roughness is observed. Figure 4.11 presents 5x5 μm 3D roughness profiles and SEM surface images for the set of samples grown at 10^{-2} mbar. It is known β-Ga_2O_3 can exhibit intrinsically rough growth on GaN due to the formation of $(\bar{2}01)$-oriented domains [6].

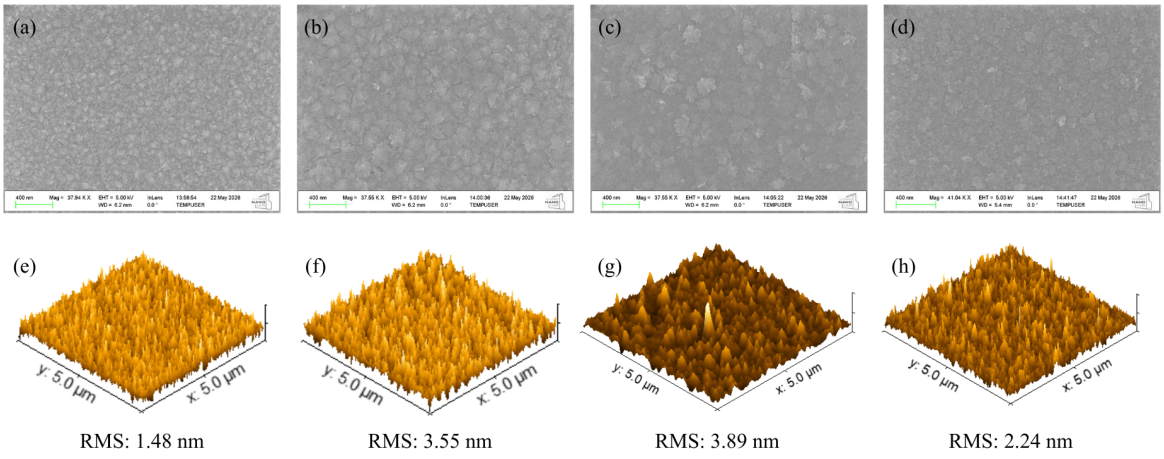

Figure 4.11: Surface morphology evolution under a fixed 10^{-2} mbar oxygen isobar across varying substrate temperatures (600°C to 800°C). Panels (a)–(d) display the SEM micrographs. Panels (e)–(h) display the 3D AFM topographies with corresponding RMS roughness values.

At a relatively low temperature of 600°C, the limited adatom surface diffusion length results in smaller domains and comparatively smooth surface morphology (Figure 4.11a and 4.11e). As the temperature increases to 750°C, so does the adatom surface diffusion length, thereby promoting domain growth and coalescence. Due to the larger domain sizes, the RMS roughness directly scales up (Figures 4.11b, 4.11f and 4.11c, 4.11g, respectively). At the highest growth temperature of 800°C, a decrease in domain size is observed (Figure 4.11d). This is attributed to a

regime in which the adatom desorption rate becomes comparable to or exceeds the incorporation rate, limiting lateral growth. This interpretation is supported by the reduced growth rate at this temperature of approximately 135 nm/h. The smaller domain size is therefore accompanied by a decrease in RMS roughness.

5 | Conclusion & Outlook

This thesis investigated the growth behaviour, structural quality and surface morphology of β-Ga_2O_3 thin films deposited via Pulsed Laser Deposition on c-plane sapphire and GaN-on-sapphire templates. Growth conditions, particularly temperature and pressure, were varied to determine critical thin-film growth relationships.

At fixed oxygen pressures, the thin-film growth rate decreases with increasing temperature for both substrate types. It was argued that elevated temperatures accelerate desorption and the decomposition of Ga_2O_3 to volatile gallium suboxide (Ga_2O) species. Furthermore, low-temperature depositions (500°C-550°C) produced a sharp increase in growth rate. The limited thermal energy constrained the surface diffusion length of adatoms, resulting in thick, rough, amorphous samples. In general, higher oxygen pressures enhanced the growth rate by accelerating the oxidation of Ga-containing species, suppressing thermal decomposition, and shifting desorption-dominated regimes to higher temperatures.

It was proven that heteroepitaxial growth of β-Ga_2O_3 on both sapphire and GaN templates preferentially aligns along the $(\bar{2}01)$ crystal plane. Films grown on GaN templates generally exhibited a lower X-ray diffraction rocking curve Full Width Half Maximum (FWHM) values compared to those on sapphire. This is reasoned to happen due to the lower lattice mismatch between β-Ga_2O_3 and GaN. On sapphire, the highest crystalline quality (FWHM = 1.14°) required high temperatures and elevated oxygen pressures (800°at 10^{-2}). Conversely, growth on GaN degraded significantly under background vacuum pressure (10^{-6} mbar), demonstrating that a minimum oxygen supply is needed to facilitate high-quality crystallization on GaN templates.

Due to direct exposure of bare GaN templates to oxygen-rich environments, surface oxidation appeared to constrain a higher crystal quality. Therefore, a thin, two-step deposition using an inert Argon buffer layer effectively protected the GaN surface from early oxidation. This strategy successfully improved film crystallinity across all tested samples, yielding a maximum improvement of approximately 38% for films grown at 750°C under 10^{-2} mbar.

Finally, the dependence between temperature and RMS roughness was studied for samples grown on GaN template. In general terms, smoother surfaces were observed at low pressures with increasing temperature. Nevertheless, under an isobaric pressure of 10^{-2} mbar, the surface RMS roughness followed a distinct non-monotonic trend with temperature. Lower temperatures (600°C) limited adatom diffusion to form small, relatively smooth domains. Intermediate temperatures (750°C) maximized domain size and coalescence, peak-scaling the overall roughness. Finally, the highest temperatures (800°C) triggered dominant adatom desorption, which limited domain growth and effectively smoothed the film surface.

Future prospects

Several aspects of the present study warrant further investigation to consolidate and extend the observed results. While this work has laid the groundwork for the growth behaviour of β-Ga_2O_3, the limited time frame and resources offered for its production have constrained further findings.

First, systematic reproducibility tests are required to confirm the robustness of the reported trends

in both crystalline quality and surface morphology.

A deeper understanding of the role of interfacial oxidation on GaN is also essential. The extent of GaN surface oxidation under different oxygen partial pressures and background gases should be investigated in more detail, as this is expected to critically influence nucleation behaviour and ultimately the structural quality of the β-Ga_2O_3 films.

Furthermore, the dataset could be expanded by increasing the number of growth points across temperature and pressure to enable a more complete mapping of the observed trends. This would allow for a more quantitative understanding of the transition regimes governing morphology, roughness evolution, and crystalline quality.

From a process stability perspective, it is recommended to perform growth at higher oxygen pressures, where possible, to minimize fluctuations associated with low-pressure operation and improve the reproducibility of the deposition conditions.

Several strategies may be considered to further improve crystalline quality, although these may come at the expense of growth rate. These include the use of thicker buffer layers, reduction of laser fluence, adjustment of laser repetition rate or buffer layer formation in nitrogen plasma. Each of these parameters may influence adatom kinetics and nucleation behaviour, and should therefore be systematically evaluated. On the other hand, strategies aimed at increasing growth rate, such as higher fluence or increased repetition rate, may adversely affect crystallinity and should be carefully balanced against structural quality requirements.

Finally, further optimization of surface morphology and roughness could be achieved through fine-tuning of growth temperature, pressure, and buffer-layer design. In particular, approaches that enhance surface diffusion without promoting excessive island coarsening may offer a pathway toward smoother films while maintaining good crystalline quality.

Overall, the work carried with PLD has proven useful in understanding the growth of crystalline β-Ga_2O_3 thin films. Although alternative techniques offer greater industrial scalability, PLD has enabled the fundamental growth of high-quality, high-purity layers with the distinct advantage of in situ monitoring via reflection high-energy electron diffraction (RHEED). These types of studies are, furthermore, crucial to experiment and prototype highly complex materials using a relatively straightforward deposition method. As a final remark, due to the tunability of PLD, growth of alloys such as $(Al_xGa_{1-x})_2O_3$ with supplementary of-interest properties, could be investigated in an accessible manner compared to other well-known deposition techniques.

Had additional time been available, an interesting next step would have been the fabrication of simple photodetectors utilizing the GaN/β-Ga_2O_3 heterostructures integrated with appropriate metallic contacts, such as Al or Au/Ti. This would enable the evaluation of key electrical characteristics, including current-voltage (I-V) curves and spectral responsivity, to assess device performance. Furthermore, more advanced architectures, such as power devices like transistors or metal-oxide-semiconductor (MOS) structures, could be fabricated to further explore this complementary material combination. While this approach introduces more complex optimization challenges regarding doping, defect density mitigation, and device design, it would yield a significantly more detailed electrical characterization of the deposited thin films.

6 | References

[1] B.J. Baliga. Power semiconductor device figure of merit for high-frequency applications. *IEEE Electron Device Letters*, 10(10):455–457, October 1989.

[2] Noiba U. Botirova, Azamat O. Arslanov, Gofur B. Eshonkulov, Jamoliddin X. Murodov, Ra'no Sh. Sharipova, Javohir Sh. Khudoykulov, and Shavkat U. Yuldashev. Effect of SiO2 and Post-Annealed Ga2O3 Buffer Layers on Ga2O3 Thin Film Growth and Properties. *Crystal Growth & Design*, 25(18):7828–7833, September 2025.

[3] Andrei A. Bunaciu, Elena gabriela Udriştioiu, and Hassan Y. Aboul-Enein. X-Ray Diffraction: Instrumentation and Applications. *Critical Reviews in Analytical Chemistry*, 45(4):289–299, October 2015. _eprint: https://doi.org/10.1080/10408347.2014.949616.

[4] Qiong Cao, Linan He, Hongdi Xiao, Xianjin Feng, Yuanjie Lv, and Jin Ma. - Ga 2 O 3 epitaxial films deposited on epi-GaN/sapphire (0001) substrates by MOCVD. *Materials Science in Semiconductor Processing*, 77:58–63, April 2018.

[5] Rongrong Chen, Di Wang, Jie Liu, Bo Feng, Hongyan Zhu, Xinyu Han, Caina Luan, Jin Ma, and Hongdi Xiao. Ta-Doped Ga2O3 Epitaxial Films on Porous p-GaN Substrates: Structure and Self-Powered Solar-Blind Photodetectors. *Crystal Growth & Design*, 22(9):5285–5292, September 2022.

[6] Hemendra Chouhan, Edmund Dobročka, Peter Nádaždy, Milan Ťapajna, Kristína Hušeková, Ildikó Cora, Alica Rosová, Miroslav Mikolášek, Fridrich Egyenes, Javad Keshtkar, Fedor Hrubišák, Michal Sobota, Peter Šiffalovič, Dagmar Gregušová, Ondrej Pohorelec, Mateusz Wosko, Regina Paszkiewicz, and Filip Gucmann. Rotational domains and origin of improved crystal quality in heteroepitaxial $(\bar{2}01)$ β-Ga_2O_3 films grown on vicinal substrates by MOCVD. *Journal of Alloys and Compounds*, 1044:184481, November 2025.

[7] Robert W. Collins. Measurement Technique of Ellipsometry. In Hiroyuki Fujiwara and Robert W. Collins, editors, *Spectroscopic Ellipsometry for Photovoltaics: Volume 1: Fundamental Principles and Solar Cell Characterization*, pages 19–58. Springer International Publishing, Cham, 2018.

[8] Juan Manuel Conde Garrido and Josefina María Silveyra. A review of typical PLD arrangements: Challenges, awareness, and solutions. *Optics and Lasers in Engineering*, 168:107677, September 2023.

[9] Abhaya Datye and Andrew DeLaRiva. Scanning Electron Microscopy (SEM). In Israel E. Wachs and Miguel A. Bañares, editors, *Springer Handbook of Advanced Catalyst Characterization*, pages 359–380. Springer International Publishing, Cham, 2023.

[10] Hiroshi Fujioka. 8 - pulsed laser deposition (pld). In Thomas F. Kuech, editor, *Handbook of Crystal Growth (Second Edition)*, Handbook of Crystal Growth, pages 365–397. North-Holland, Boston, second edition edition, 2015.

[11] Swapnodoot Ganguly, Krishna Nama Manjunatha, and Shashi Paul. Advances in Gallium Oxide: Properties, Applications, and Future Prospects. *Advanced Electronic Materials*, 11(7):2400690, May 2025.

[12] Lauren M. Garten, Andriy Zakutayev, John D. Perkins, Brian P. Gorman, Paul F. Ndione, and David S. Ginley. Structure property relationships in gallium oxide thin films grown by pulsed laser deposition. *MRS Communications*, 6(4):348–353, December 2016.

[13] Franz J Giessibl. Advances in atomic force microscopy. *Rev. Mod. Phys.*, 75(3), 2003.

[14] Adawiya J. Haider, Taif Alawsi, Mohammed J. Haider, Bakr Ahmed Taha, and Haydar Abdulameer Marhoon. A comprehensive review on pulsed laser deposition technique to effective nanostructure production: trends and challenges. *Optical and Quantum Electronics*, 54(8):488, August 2022.

[15] S. J. Hao, M. Hetzl, F. Schuster, K. Danielewicz, A. Bergmaier, G. Dollinger, Q. L. Sai, C. T. Xia, T. Hoffmann, M. Wiesinger, S. Matich, W. Aigner, and M. Stutzmann. Growth and characterization of -Ga2O3 thin films on different substrates. *Journal of Applied Physics*, 125(10):105701, March 2019.

[16] George F. Harrington and José Santiso. Back-to-Basics tutorial: X-ray diffraction of thin films. *Journal of Electroceramics*, 47(4):141–163, December 2021.

[17] Masataka Higashiwaki, Kohei Sasaki, Hisashi Murakami, Yoshinao Kumagai, Akinori Koukitu, Akito Kuramata, Takekazu Masui, and Shigenobu Yamakoshi. Recent progress in Ga2O3 power devices. *Semiconductor Science and Technology*, 31(3):034001, January 2016.

[18] Lin Huang, Huili Tang, Chaoyi Zhang, Peng Sun, Qiancheng Fang, Feng Wu, Ping Luo, Bo Liu, and Jun Xu. Growth of gallium oxide bulk crystals: a review. *The European Physical Journal Special Topics*, 234(2):231–271, May 2025.

[19] J.A. Woollam. Interaction of light and materials. https://www.jawoollam.com/resources/ellipsometry-tutorial/interaction-of-light-and-materials, 2025. Ellipsometry Tutorial. Accessed: 2026-06-03.

[20] Daniel Johnson, Nidal Hilal, and W. Richard Bowen. Basic Principles of Atomic Force Microscopy. In *Atomic Force Microscopy in Process Engineering*, pages 1–30. Elsevier, 2009.

[21] Jevgenijs Kaupužs, Arturs Medvids, Pavels Onufrijevs, and Hidenori Mimura. Origin of n-type conductivity in ZnO crystal and formation of Zn and ZnO nanoparticles by laser radiation. *Optics & Laser Technology*, 111:121–128, April 2019.

[22] Weijiang Li, Xiang Zhang, Ruilin Meng, Jianchang Yan, Junxi Wang, Jinmin Li, and Tongbo Wei. Epitaxy of III-Nitrides on -Ga2O3 and Its Vertical Structure LEDs. *Micromachines*, 10(5):322, May 2019.

[23] Zihao Li, Xiangxiang Gao, Yuelong Feng, Dongsheng Cui, Jian Li, Zhenhua Lin, Yue Hao, and Jingjing Chang. Gallium Oxide RRAM: Materials, Fundamentals and Applications. *Advanced Materials Technologies*, page e02218, January 2026.

[24] Yougui Liao. Practical electron microscopy and database. *An Online Book*, 3:1412, 2006.

[25] Xiaocui Ma, Rui Xu, Yang Mei, Leiying Ying, Baoping Zhang, and Hao Long. Crystalline anisotropy of -Ga2O3 thin films on a c-plane GaN template and a sapphire substrate. *Semiconductor Science and Technology*, 37(3):035003, January 2022.

[26] Kannan Malaichamy. Scanning Electron Microscopy: Principle, Components and Applications. pages 81–92. March 2018.

[27] Ivan V Markov. *Crystal Growth for Beginners: Fundamentals of Nucleation, Crystal Growth and Epitaxy*. WORLD SCIENTIFIC, 3 edition, March 2017.

[28] M. M. Muhammed, M. Peres, Y. Yamashita, Y. Morishima, S. Sato, N. Franco, K. Lorenz, A. Kuramata, and I. S. Roqan. High optical and structural quality of GaN epilayers grown on (2¯01) -Ga2O3. *Applied Physics Letters*, 105(4):042112, July 2014.

[29] Shinji Nakagomi and Yoshihiro Kokubun. Crystal orientation of -Ga2O3 thin films formed on *c*-plane and *a*-plane sapphire substrate. *Journal of Crystal Growth*, 349(1):12–18, June 2012.

[30] Hartwin Peelaers and Chris G. Van de Walle. Brillouin zone and band structure of -Ga2O3. *physica status solidi (b)*, 252(4):828–832, 2015. _eprint: https://onlinelibrary.wiley.com/doi/pdf/10.1002/pssb.201451551.

[31] Hartwin Peelaers and Chris G. Van De Walle. Sub-band-gap absorption in Ga2O3. *Applied Physics Letters*, 111(18):182104, October 2017.

[32] N.J. Podraza and G.E. Jellison. Ellipsometry. In *Encyclopedia of Spectroscopy and Spectrometry*, pages 482–489. Elsevier, 2017.

[33] Udo W. Pohl. *Epitaxy of Semiconductors: Introduction to Physical Principles*. Graduate Texts in Physics. Springer Berlin Heidelberg, Berlin, Heidelberg, 2013.

[34] A.A.G. Requicha, S. Meltzer, F.P.T. Arce, J.H. Makaliwe, H. Siken, S. Hsieh, D. Lewis, B.E. Koel, and M.E. Thompson. Manipulation of nanoscale components with the AFM: principles and applications. In *Proceedings of the 2001 1st IEEE Conference on Nanotechnology. IEEE-NANO 2001 (Cat. No.01EX516)*, pages 81–86, October 2001.

[35] Richard E. Russo, X.L. Mao, J. Yoo, and J.J. Gonzalez. Laser ablation. In *Laser-Induced Breakdown Spectroscopy*, pages 41–70. Elsevier, 2007.

[36] J. Schou. Physical aspects of the pulsed laser deposition technique: The stoichiometric transfer of material from target to film. *Applied Surface Science*, 255(10):5191–5198, March 2009.

[37] Mathias Schubert, Alyssa Mock, Megan Stokey, Viktor Rindert, Nerijus Armakavicius, and Vanya Darakchieva. Characterization of semiconductors by spectroscopic ellipsometry. In *Comprehensive Semiconductor Science and Technology*, pages 495–539. Elsevier, 2025.

[38] Roland Seitz. Spectroscopic Ellipsometry of Compound Semiconductors: AlGaN/GaN Hetero-Structures, 2005.

[39] Dahee Seo, Sunjae Kim, Hyeong-Yun Kim, Dae-Woo Jeon, Ji-Hyeon Park, and Wan Sik Hwang. Heteroepitaxial Growth of Single-Crystalline -Ga_2 O_3 on GaN/Al_2 O_3 Using MOCVD. *Crystal Growth & Design*, 23(10):7090–7094, October 2023.

[40] E Serquen, F Bravo, Z Chi, L A Enrique, K Lizárraga, C Sartel, E Chikoidze, and J A Guerra. Impact of c- and m- sapphire plane orientations on the structural and electrical properties of -Ga_2 O_3 thin films grown by metal-organic chemical vapor deposition. *Journal of Physics D: Applied Physics*, 57(49):495106, December 2024.

[41] Nick A. Shepelin, Zahra P. Tehrani, Natacha Ohannessian, Christof W. Schneider, Daniele Pergolesi, and Thomas Lippert. A practical guide to pulsed laser deposition. *Chemical Society Reviews*, 52(7):2294–2321, 2023.

[42] Abhishek Kumar Singh, Anderson Janotti, Matthias Scheffler, and Chris G. Van De Walle. Sources of Electrical Conductivity in SnO 2. *Physical Review Letters*, 101(5):055502, July 2008.

[43] Oleksiy Slobodyan, Jack Flicker, Jeramy Dickerson, Jonah Shoemaker, Andrew Binder, Trevor Smith, Stephen Goodnick, Robert Kaplar, and Mark Hollis. Analysis of the dependence of critical electric field on semiconductor bandgap. *Journal of Materials Research*, 37(4):849–865, February 2022.

[44] M. Slomski, N. Blumenschein, P. P. Paskov, J. F. Muth, and T. Paskova. Anisotropic thermal conductivity of -Ga2O3 at elevated temperatures: Effect of Sn and Fe dopants. *Journal of Applied Physics*, 121(23):235104, June 2017.

[45] St Paul's School. Interaction volume. https://intranet.stpaulsschool.org.uk/halley-research-community/scanning-electron-microscope-sem/interaction-volume, 2015. Halley Research Community: Scanning electron microscope (SEM). Accessed: 2026-06-03.

[46] G B Stringfellow. Epitaxy. *Reports on Progress in Physics*, 45(5):469–525, May 1982.

[47] Wanxin Sun. Principles of Atomic Force Microscopy. In Jiye Cai, editor, *Atomic Force Microscopy in Molecular and Cell Biology*, pages 1–28. Springer, Singapore, 2018.

[48] Tobias Særkjær, Thue Christian Thann, Sergej Schuwalow, and Peter Krogstrup. Collective formation of misfit dislocations at the critical thickness for equilibrium nanowire heterostructures. *Journal of Crystal Growth*, 622:127400, November 2023.

[49] Noriharu Takada, Noriyuki Taoka, Taishi Yamamoto, Akio Ohta, Nguyen Xuan Truyen, Hisashi Yamada, Tokio Takahashi, Mitsuhisa Ikeda, Katsunori Makihara, Mitsuaki Shimizu, and Seiichi Miyazaki. Impact of remote plasma oxidation of a GaN surface on photoluminescence properties. *Japanese Journal of Applied Physics*, 58(SE):SEEC02, June 2019.

[50] Dat Tran. *Thermal conductivity of wide and ultra-wide bandgap semiconductors*, volume 2334 of *Linköping Studies in Science and Technology. Dissertations*. Linköping University Electronic Press, Linköping, October 2023.

[51] Patrick Vogt, Felix V. E. Hensling, Kathy Azizie, Celesta S. Chang, David Turner, Jisung Park, Jonathan P. McCandless, Hanjong Paik, Brandon J. Bocklund, Georg Hoffman, Oliver Bierwagen, Debdeep Jena, Huili G. Xing, Shin Mou, David A. Muller, Shun-Li Shang, Zi-Kui Liu, and Darrell G. Schlom. Adsorption-controlled growth of Ga2O3 by suboxide molecular-beam epitaxy. *APL Materials*, 9(3):031101, March 2021.

[52] Bert Voigtländer. *Atomic Force Microscopy*. NanoScience and Technology. Springer International Publishing, Cham, 2019.

[53] Aadil Waseem, Zhongjie Ren, Hsien-Chih Huang, Kristen Nguyen, Xihang Wu, and Xiuling Li. A Review of Recent Progress in -Ga2O3 Epitaxial Growth:

Effect of Substrate Orientation and Precursors in Metal–Organic Chemical Vapor Deposition. *physica status solidi (a)*, 220(8):2200616, 2023. _eprint: https://onlinelibrary.wiley.com/doi/pdf/10.1002/pssa.202200616.

[54] H. von Wenckstern, M. Andreassen, and K. G. Both. 2.08 - Fundamentals of pulsed laser deposition, advanced developments and implementation of combinatorial material synthesis, and its application to the growth of Ga2O3 and related alloys. In Roberto Fornari, editor, *Comprehensive Semiconductor Science and Technology (Second Edition)*, pages 225–266. Elsevier, Oxford, second edition edition, 2025.

[55] S. Wicklein, A. Sambri, S. Amoruso, X. Wang, R. Bruzzese, A. Koehl, and R. Dittmann. Pulsed laser ablation of complex oxides: The role of congruent ablation and preferential scattering for the film stoichiometry. *Applied Physics Letters*, 101(13):131601, September 2012.

[56] P. R. Willmott and J. R. Huber. Pulsed laser vaporization and deposition. *Reviews of Modern Physics*, 72(1):315–328, January 2000.

[57] Chris J.H. Wort and Richard S. Balmer. Diamond as an electronic material. *Materials Today*, 11(1-2):22–28, January 2008.

[58] Chao Wu, Guang Zhang, Jinhua Jia, Haizheng Hu, Fengmin Wu, Shunli Wang, and Daoyou Guo. Highly Polarization-Deep-Ultraviolet-Sensitive -Ga2O3 Epitaxial Films by Disrupting Rotational Symmetry and Encrypted Solar-Blind Optical Communication Application. *The Journal of Physical Chemistry Letters*, 15(14):3828–3834, April 2024.

[59] A. R. A. Zauner, M. a. C. Devillers, P. R. Hageman, P. K. Larsen, and S. Porowski. Spectroscopic Ellipsometry on GaN: Comparison Between Hetero-epitaxial Layers and Bulk Crystals. *Materials Research Society Internet Journal of Nitride Semiconductor Research*, 3:e17, January 1998.

[60] Jiaye Zhang, Jueli Shi, Dong-Chen Qi, Lang Chen, and Kelvin H. L. Zhang. Recent progress on the electronic structure, defect, and doping properties of Ga2O3. *APL Materials*, 8(2):020906, February 2020.

[61] Weilie Zhou, Robert Apkarian, Zhong Lin Wang, and David Joy. Fundamentals of Scanning Electron Microscopy (SEM). In Weilie Zhou and Zhong Lin Wang, editors, *Scanning Microscopy for Nanotechnology: Techniques and Applications*, pages 1–40. Springer, New York, NY, 2007.

[62] J. Åhman, G. Svensson, and J. Albertsson. A Reinvestigation of -Gallium Oxide. *Acta Crystallographica Section C*, 52(6):1336–1338, 1996. _eprint: https://onlinelibrary.wiley.com/doi/pdf/10.1107/S0108270195016404.

A | Specifications of characterization tools

Bruker D8 Discover XRD

X-ray diffraction measurements were performed using a Bruker D8 Discover diffractometer. The system was equipped with a Cu Kα radiation source (λ = 1.5418 Å) operating at a voltage of 40 kV and a current of 40 mA. The slit width was set to 0.5 mm. High-resolution scans were acquired in the 2θ-ω and RC configuration. The 2θ-ω diffraction patterns were recorded over a 2θ range of 10° to 90° with a step size of 0.01° and a dwell time of 0.2 s per step. The RC scans were recorded over a ω range of 6° to 12° with a step size of 0.0065° and a dwell time of 1 s per step. Data analysis and FWHM identification were carried out using the software Origin.

Woolam RC2 Ellipsometer

Spectroscopic ellipsometry data were collected using a J.A. Woolam RC2 dual-rotating compensator ellipsometer. Amplitude (Ψ) and phase (Δ) spectra were recorded over the entire available wavelength range at multiple angles of incidence, specifically 55°, 60°, 65°, and 70°. Optical modelling and layer thickness determination were performed using the CompleteEASE software package. The experimental data were fitted using a Cauchy, Lorentz and EMA optical models to minimize the Mean Squared Error (MSE).

Bruker AFM Icon

Surface topography and roughness analysis were conducted via Atomic Force Microscopy using a Bruker Dimension Icon system. Images were captured in Tapping Mode mode under ambient conditions using TESPA-V2 silicon probes with a nominal tip radius of 7 nm and a spring constant of 37 N/m. Scan sizes of 5×5 μm^2 were acquired at a scan rate of 0.2 Hz. Image processing and root-mean-square (RMS) roughness calculation were performed using Gwyddion software.

Zeiss Gemini SEM

Surface morphology and microstructural cross-sections were characterized using a Zeiss Gemini 500 field-emission scanning electron microscope (FE-SEM). High-resolution images were acquired at an accelerating voltage of 5 kV and a working distance of approximately 5 mm to 6 mm. Signals were collected using the InLens / Secondary Electron (SE2) / Backscattered Electron (AsB) detector depending on the required contrast and resolution.

B | RHEED in-situ monitoring

RHEED was used as a way of identifying the speed at which nucleation occurs on sapphire and GaN substrates, as well as to understand how the introduction of the buffer layer altered the nucleation process. Furthermore, this resource enable the identification of growth modes for the measured films. Due to the late availability of this resource, only selected growth runs could be monitored.

The images obtained with RHEED showcase characteristic diffraction patterns, which can bring light to which growth mode is happening. From literature [41], the correlation of diffraction patterns with growth modes is understood. These can be observed in Figure B.1.

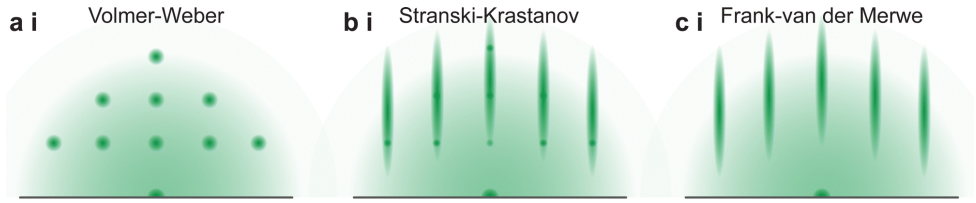

Figure B.1: Identifying RHEED pattern structures of the three thin-film growth modes [41].

Taking the growth at 750°C at 10^{-2} mbar as reference, the nucleation process on GaN, on sapphire, and with an Ar buffer can be investigated. The images taken before, during and after the growth process can be observed in Figure B.2. It must be noted that image post-processing has been done to be able to distinguish more intense patterns.

In general terms, a van-der Merwe growth mode first dominated, indicated by the rod-like patterns obtained at early growth stages. It is clear, especially for Figure B.2b, that a Volmer-Weber-like mode follows, due to the formation of $(\bar{2}01)$ oriented domains. Differences between substrates are inconclusive, and further experimentation is required.

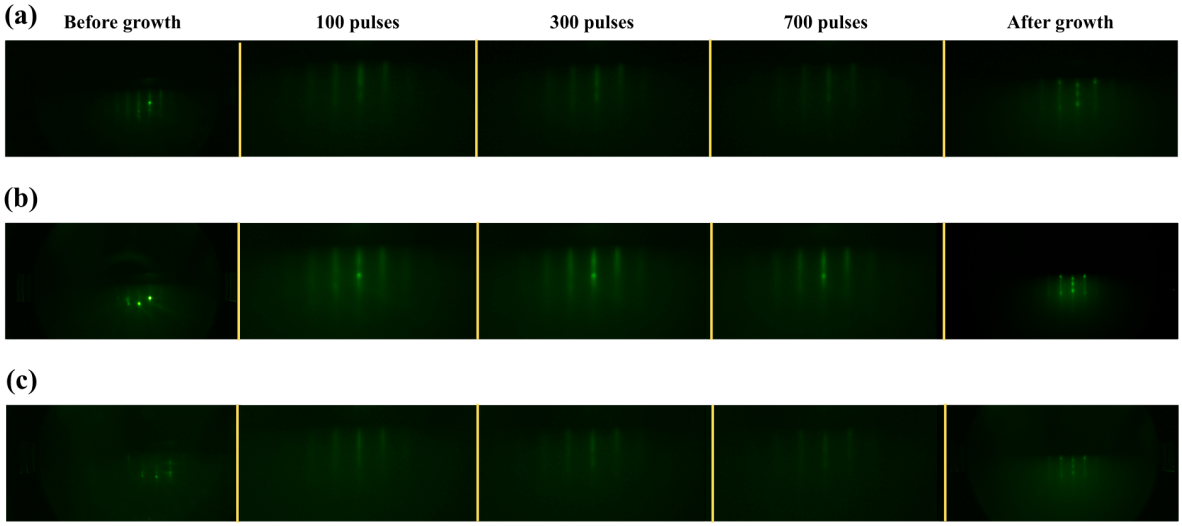

Figure B.2: RHEED diffraction patterns obtained for (a) growth on GaN template, (b) growth on GaN template with Ar-grown buffer, and (c) growth on sapphire.